

# Free-fall experiments of volcanic ash particles

## using a 2D video disdrometer

Sung-Ho Suh<sup>1</sup> (Email: [suhsh1215@pukyong.ac.kr](mailto:suhsh1215@pukyong.ac.kr))

Masayuki Maki<sup>2\*</sup> (Email: [maki@gm.kagoshima-u.ac.jp](mailto:maki@gm.kagoshima-u.ac.jp))

Masato Iguchi<sup>3</sup> (Email: [iguchi@svo.dpri.kyoto-u.ac.jp](mailto:iguchi@svo.dpri.kyoto-u.ac.jp))

Dong-In Lee<sup>1</sup> (Email: [leedi@pknu.ac.kr](mailto:leedi@pknu.ac.kr))

Akihiko Yamaji<sup>4</sup> (Email: [yamaji@jwa.or.jp](mailto:yamaji@jwa.or.jp))

Tatsuya Momotani<sup>4</sup> (Email: [momotani@jwa.or.jp](mailto:momotani@jwa.or.jp))

Institutional addresses:

<sup>1</sup>Department of Environmental Atmospheric Sciences, Pukyong National University, Namgu, Busan, Republic of Korea

<sup>2</sup>Research and Education Center for Natural Hazards, Kagoshima University, Korimoto, Kagoshima, Japan

<sup>3</sup>Sakurajima Volcano Research Center, Disaster Prevention Research Institute, Kyoto University, Sakurajima, Kagoshima, Japan

<sup>4</sup>Japan Weather Association, Higashi-Ikebukuro, Toshima-ku, Tokyo, Japan

\* Corresponding author: Masayuki Maki ([maki@gm.kagoshima-u.ac.jp](mailto:maki@gm.kagoshima-u.ac.jp))

Key Points: Volcanic ash, 2DVD, aerodynamic properties, laboratory experiments

21 The English in this document has been checked by at least two professional editors, both native  
22 speakers of English. For a certificate, please see:

23

24 <http://www.textcheck.com/certificate/7pU3Ux>

25

26

27        **Abstract**

28        Information of aerodynamic parameter of volcanic ash particles, such as terminal velocity, axis  
29 ratio, and canting angle, which are necessary for quantitative ash-fall estimations with weather radar.  
30 In this study, free-fall experiments of volcanic ash particle were accomplished using a two-dimensional  
31 video disdrometer under controlled conditions.

32        Samples containing a rotating symmetric axis were selected and divided into five types according  
33 to shape and orientation: oblate spheroid with horizontal rotating axis (OH), oblate spheroid with  
34 vertical axis (OV), prolate spheroid with horizontal rotating axis (PH), prolate spheroid with vertical  
35 rotating axis (PV), and sphere (Sp). The horizontally (OH and PH) and vertically (OV and PV) oriented  
36 particles were present in proportions of 76% and 22%, and oblate and prolate spheroids were in  
37 proportions of 76% and 24%, respectively. The most common shape type was OH (57%).

38        The terminal velocities of OH, OV, PH, PV, and Sp were obtained analyzing 2DVD data. The  
39 terminal velocities of PV were highest compared to those of other particle types. The lowest terminal  
40 velocities were found in OH particles. It is interesting the terminal velocities for OH decreased rapidly  
41 in the range  $0.5 < D < 1$  mm corresponding to the decrease in axis ratio (i.e., smaller the particle, the  
42 flatter the shape). The axis ratios of all particle types except Sp were found to be converged to 0.94 at  
43  $D > 2$  mm.

44        The histogram of canting angles followed unimodal and bimodal distributions with respect to  
45 horizontally and vertically oriented particles, respectively. The mean values and the standard deviation  
46 of entire particle shape types were close to  $0^\circ$  and  $10^\circ$ , respectively under calm atmospheric conditions.

## 1. Introduction

Volcanic eruptions are considered one of the most severe types of natural phenomena, and can lead to human casualties and property damage. Ash consists of very fine-grained fragments, volume-equivalent spherical particle diameter ( $D$  in  $\mu\text{m}$ ) is generally smaller than  $200 \mu\text{m}$ , and these are generally dominated by broken glass shards rather than crystal and lithic fragments. Wilson et al. (2012) overview for the ash effects on critical infrastructures such as ash fall and acid rain. Hilman et al. (2012) investigate the effect ash particles on human health in case of Sakurajima volcanic eruptions. More comprehensive descriptions on the volcanic ash impacts on society is found in Sigurdsson et al. (2015) and Wilson et al. (2015). Following an eruption, fine airborne volcanic ash flows for several tens of kilometers, which can cause major problems by increasing aviation traffic (e.g., Bonadonna et al., 2012; Langmann et al., 2012); this was seen after the eruption of Eyjafjallajökull volcano in Iceland during the period April 14–21, 2010, for example Bonadonna et al. (2011). From the viewpoint of volcanological hazard reduction, accurate description of transport and deposition in the numerical forecasting model of volcanic ash clouds are vitally important (Poulidis et al., 2017).

Terminal fall velocity ( $V_T$ ) of a particle is affected by its shape, density, size, and atmospheric properties. Wilson and Huang (1979), Dellino (2005), and Coltelli et al. (2008) introduced the influence of ash particle shapes on its  $V_T$ . Haider and Levenspile (1989) and Ganser (1993) analyzed  $V_T$  of volcanic ash particle on the drag coefficient ( $C_D$ ) which is dependent on the particle shape and atmospheric condition. Transport and sedimentation of volcanic ash are complex processes, and the residence time and fall velocity of ash is critically dependent on particle size (Bonadonna et al., 1998), where with respect to the latter, smaller particles could be flowing in the atmosphere further from the vent.

Aerodynamic properties are important for safe aviation, and for studying the effects of volcanic ash on climate change, since these parameters determine the residence time of ash particles in the

71 atmosphere (e.g., Folch et al., 2009). The  $V_T$  of particles vary widely due to their irregular shapes and  
72 material components (e.g., Wilson, 1972; Harris and Rose, 1983; Bonadonna et al., 2011, Maki et al.,  
73 2016). Bonadonna et al. (2011) analyzed  $V_T$  of volcanic ash particle with various particle density ( $\rho_s$ )  
74 from 990 to 2738 kg m<sup>-3</sup> and Maki et al. (2016) summarized the list of various  $V_T$  relationships  
75 suggested by previous studies. Volcanic ash particles have a range of shapes, and this presents a major  
76 challenge when analyzing their characteristics. Recently, the irregularity of volcanic ash particles was  
77 analyzed in detail based on the features of various regular particles, such as cubes, cylinders, and disks  
78 (Bagheri and Bonadonna, 2016), using a computed tomography (CT) scanner (Dioguardi et al., 2017;  
79 Garboczi and Bullard, 2017).

80 There are two approaches to studying these aerodynamic properties. The first approach is  
81 theoretical, where a numerical simulation model is used to calculate terminal velocities, drag force,  
82 and Reynolds number (Re); examples of this approach can be found in Happel and Brenner (2012).  
83 The second approach is related to experimental research, in which the aforementioned relationships  
84 are determined experimentally. For instance, Bagheri et al. (2013) and Bagheri and Bonadonna (2016)  
85 analyzed the aerodynamic features of irregular shaped ash particle from the free fall experiments.  
86 Dioguardi et al. (2018) suggested a new model of fluid drag for irregular shaped particles using various  
87 previous researches. Since the aerodynamic feature depends on atmospheric condition and it can affect  
88 the retrieval of  $V_T$ , it would be suggested that it can be analyzed through the free-fall laboratory  
89 experiments for the following main reasons: 1) there is few chance to measure natural falling ash  
90 particles. 2) it can be possible to control the size of ash particle in the free fall experiments. 3) and can  
91 reduce wind effect in the experiments.

92 The present study applies the second approach (experimental research) to clarify the physical  
93 characteristics of volcanic ash particles analyzing the experimental data. The rest of this paper is  
94 organized as follows. Section 2 describes the free-fall experiments of ash particles and methods of

95 analysis. Section 3 presents the results of the free fall experiments. Section 4 is discussions and section

96 5 summarizes the results.

97

98        **2. Data and Methods**

99

100        **a. Two dimensional (2D) video disdrometer**

101        The 2D video disdrometer (2DVD) was developed by Joanneum Research (Graz, Austria) to detect  
102        single raindrop particles, and the instrument has been modified to cover the errors caused by turbulence  
103        effects (Nešpor et al., 2000). The device is able to observe the shape,  $V_T$ , and  $\beta$  of a single particle  
104        using optical light. The ability to analyze a single particle is a significant advantage compared to other  
105        disdrometers, such as the Joss-Waldvogel disdrometer (Joss and Waldvogel, 1967), the Precipitation  
106        Occurrence Sensor System (Sheppard, 1990), and Parsivel (Löffler-Mang and Joss 2000). For instance,  
107        Parsivel considers a fixed measurement area without any consideration of particle shape (e.g., Tokay  
108        et al., 2014), while 2DVD observes particles by passing them through a 100 cm<sup>2</sup> observation area  
109        consisting of two light sources and reflecting mirrors and two cameras, one set 6.2 mm above the other,  
110        and collects data with a resolution of 630 pixels; this results in a pixel size of 0.2 mm at 55 kHz (Kruger  
111        and Krajewski, 2002). Particles passing through the observation area yield shape information  
112        according to the radiation intensity of the light sources, which is helpful for calculation of  $\gamma$  and  $\beta$ . The  
113         $V_T$  of particles is calculated using the height difference between the two cameras. Based on these  
114        advantages, the oscillation and particle shape of raindrops can be analyzed by 2DVD (Thurai and  
115        Bringi, 2005). Böhm (1989) analyzed the aerodynamic properties of an irregular hydrometeor and  
116        Huang et al. (2010, 2015) used 2DVD to analyze the features of irregularly shaped snow. There have  
117        been few previous aerodynamic analyses of volcanic ash particles performed using 2DVD, which is  
118        able to detect and analyze volcanic ash particles with a range of irregular shapes. Thus, 2DVD offers  
119        a unique approach as a new observation strategy.

120

121

122 **b. Definition of particle shape type**

123 Volcanic ash particles have various shapes that can be detected by 2DVD (Fig. 1). In the case of  
124 raindrops, the DSD is dependent upon the break-up and coalescence processes occurring via up and  
125 downdrafts, since the forces of gravity and buoyancy can easily affect raindrop shapes (Rosenfeld and  
126 Ulbrich, 2003). However, solid particles do not readily change shape when falling without the  
127 influence of forces such as collision. It is thus inferred that many particle shapes would be found in the  
128 atmosphere, and that it would be possible to define and classify each particle shape type if we were  
129 able to accurately detect a single particle. Thus, the range of  $\gamma$  for solid particles would be expected to  
130 be wide compared to that of raindrops, and various values of  $V_T$  and  $\beta$  would likely be observed. The  
131  $\gamma_x$  of a particle is defined as the ratio of height to width for the observation direction  $x$ , and its  
132 representative value is calculated using the geometric means of the two  $\gamma$  ( $\gamma_1, \gamma_2$ ) detected by cameras  
133 1 and 2, respectively (Eq. 1):

134

$$\gamma_{1(2)} = \frac{\text{Height}_{1(2)}}{\text{Width}_{1(2)}}, \quad \gamma = \sqrt{\gamma_1 \gamma_2}$$

135

136

137 Eq. (1).

138

139 The difference in angle between the rotating symmetric axis and vertical axis is defined as  $\beta$ . The  
140 counter-clockwise (clockwise) movement of the rotating symmetric axis has a positive (negative) value  
141 and the entire range is  $180^\circ$  (from  $-90^\circ$  to  $90^\circ$ ) with  $0^\circ$  as the center.

142 It is necessary to consider the true axis ratio ( $\gamma_T$ ) to correctly define the particle shape (Fig. 2). The  
143 apparent axis ratio ( $\gamma_A$ ) considers the effect of  $\beta$  but the  $\gamma_T$  does not. The 2D coordinates ( $x, z$ ) of the  
144 particle shape with  $\beta$  are defined as follows:



145

146

$$x_A = r \cos(\theta + \beta), \quad z_A = r \sin(\theta + \beta)$$

147

148

$$x_T = r \cos\theta, \quad z_T = r \sin\theta$$

149

150

151

152

153

where subscript A is the coordinate of the original data coordinate considering the  $\beta$  and subscript T is the modified data coordinate. The symbol  $r$  refers to the length from the data point to the center and the symbol  $\theta$  represents the degrees of data coordinates from the positive x axis, which range between  $0^\circ$  and  $180^\circ$ . In this paper,  $\gamma$  stands for  $\gamma_A$  for convenience.

154

155

156

157

158

159

160

161

162

163

An objective criterion for particle shape type was considered since particle shapes can be highly diverse and irregular (e.g., Bagheri and Bonadonna, 2016; Dioguardi et al., 2017; Garboczi and Bullard, 2017; Dioguardi et al., 2018). In the case of irregular particles, the  $\gamma$  can change according to the observation direction; however, any criterion should be able to define the particle shape types strictly and reliably. To solve this problem, particles with a rotating symmetric axis were the main target of the present study. Therefore, we considered oblate spheroid (O), prolate spheroid (P), and sphere (Sp), which all have a rotating symmetric axes. Among these particle types, the major axes of the oblate and prolate spheroids could be horizontally (H) and vertically (V) oriented with respect to the ground, respectively. Thus, the various particle shapes were divided into five types as follows; OH, OV, PH, PV, and Sp.

164

165

166

167

168

To define these particle shape types, a strict definition of the  $\gamma_T$  is required, which can be calculated from the  $\beta$ . As with the  $\gamma$ , the two  $\beta$  values are automatically calculated by 2DVD. In the case where the  $\beta$  is assumed as  $0^\circ$ , the rotating symmetric axis for OH and PV can be defined, since it is observed for any observation direction parallel to the ground. However, in the case of OV and PH particles, the rotating symmetric axis cannot be defined when the observation direction is parallel. In the case where

169 the  $\beta$  is not  $0^\circ$ ,  $\gamma_T$  for all particle shape types would not change when oscillation occurs in a direction  
170 orthogonal to the observation direction, but it is difficult to estimate both  $\gamma_T$  and  $\beta$  when particle  
171 oscillation appears in a direction parallel to the observation direction. The ability to restore the  $\gamma_T$  and  
172  $\beta$  relative to this observation direction is limited, which is one of the main disadvantages of the 2D  
173 observation strategy.

174 Based on these facts, a major  $\beta$  was selected based on the following reasoning: i) a  $\beta$  for the  
175 observation direction with lower (higher)  $\gamma_T$  for OH (PV) is selected. ii) in the case of OV (PH), for  
176 which the rotating symmetric axis was observed for only one observation direction,  $\beta$  was considered  
177 where the value of  $\beta$  had a higher (lower)  $\gamma_T$  than that of the other observation direction. Therefore,  $\beta$   
178 with a lower (higher)  $\gamma_T$  in two observation directions for the case of an oblate (prolate) particle was  
179 considered as a meaningful value. The perfect sphere could not have their value of  $\beta$  determined  
180 theoretically, because there is the possibility of a rotating symmetric axis in any direction.

181 Based on the definition of  $\beta$  (Fig. 2), the perfect condition with respect to ellipsoids is satisfied  
182 when  $|\beta| = 0^\circ (90^\circ)$  for OH and PV (OV and PH); these values are defined as the center values. However,  
183 2DVD calculated that the  $\beta$  for each particle shape type was concentrated around  $|\beta| = 0^\circ (90^\circ)$  with  
184 respect to horizontally (vertically) oriented particles, which correspond to OH and PH (OV and PV).  
185 Furthermore, analysis of particles with an orthogonal center angle from  $0^\circ$  is difficult, since they have  
186 two center angles ( $\pm 90^\circ$ ). To address observation errors and enhance the convenience of analysis, all  
187 center angles were set to  $|\beta| = 0^\circ$  and modified to give the representative canting angle,  $\beta_R$ , using the  
188 following equation:

189

190

$$\beta_R = \beta - \beta_0$$

191

192 where  $\beta_0$  is the orienting angle, defined by the central angle of oscillation. In the case of vertically  
193 oriented particles (OV and PV),  $\beta_0$  could be defined as  $\pm 90^\circ$ . The sign of  $\beta_0$  follows that of  $\beta$ .

194 After removing  $\beta$ , each particle shape was defined using  $\gamma_T$  (Table 1). Note that a 10% bias range  
195 was allowed, to take observational error into account. For example, a particle was considered as a  
196 sphere when  $0.9 < \gamma_T < 1.1$ , which is an applied 10% bias range from  $\gamma_T = 1$ . In addition, the particle  
197 types OH and PV (OV and PH) were classified when the value of  $|\gamma_1 - \gamma_2|$  was smaller (larger) than  
198  $0.1\gamma_T$ , to consider particles with only a rotating symmetric axis.

199

200

### 201 **c. Calculate the terminal velocity for the various particle shape types**

202 The  $V_T$  of volcanic ash is required to estimate the  $R_A$  ( $\text{kg m}^{-2} \text{s}^{-1}$ ) on the ground where this depends  
203 on atmospheric density ( $\rho_g$  in  $\text{g cm}^{-3}$ ),  $T$ ,  $Re$ ,  $C_D$ ,  $D$ ,  $\rho_s$ , and its shape. Kunii and Levenspiel (1969)  
204 developed a theoretical  $V_T$  equation:

205

$$206 \quad V_T = \left( \frac{4(\rho_s - \rho_g)gD}{3\rho_g C_D} \right)^{0.5} \quad (10^0 < Re < 10^4)$$

207 Eq. (2)

208

209 Later, Suzuki (1983) developed a theoretical  $V_T$  equation for tephra. Bonadonna et al. (2011) then  
210 modified the theoretical  $V_T$  equation suggested by Kunii and Levenspiel (1969) with observed ash data,  
211 which implied that the result of the theoretical  $V_T$  equation could be unsuitable for non-spherical  
212 particles. Based on these equations, various  $C_D$  equations considering non-spherical particles were  
213 subsequently developed. Tran-Cong et al. (2004) developed a new equation for  $C_D$  using the function

214 of circularity and Hölzer and Sommerfeld (2008) introduced a progressed  $C_D$  equation considering two  
 215 types of sphericity: lengthwise ( $\Phi_{||}$ ) and crosswise ( $\Phi_{\perp}$ ). This equation is as follows:

216

$$217 \quad C_D = \frac{8}{Re} \frac{1}{\sqrt{\Phi_{||}}} + \frac{16}{Re} \frac{1}{\sqrt{\Phi}} + \frac{3}{\sqrt{Re}} \frac{1}{\Phi^{3/4}} + 0.42 \times 10^{0.41(-\log(\Phi))^{0.2}} \frac{1}{\Phi_{\perp}}$$

218

Eq. (3)

219

220 The  $Re$  is defined as:

221

$$222 \quad Re = \frac{\rho_g V_T D}{\mu}$$

223

Eq. (4)

224

225 where  $\mu$  is the dynamic viscosity ( $\text{kg m}^{-1} \text{s}^{-1}$ ), which we assumed to be  $1.983 \times 10^{-5}$  based on  
 226 atmospheric conditions at a  $T$  of  $25 \text{ }^\circ\text{C}$ . Three types of sphericity were defined as follows:

227

$$228 \quad \Phi = \frac{\pi D^2}{SA}$$

229

Eq. (5)

230

231 where  $SA$  is the surface area of the particle ( $\text{mm}^2$ ). The lengthwise sphericity is defined as the ratio  
 232 between the cross-sectional area of the volume-equivalent sphere and the difference between half the  
 233 surface area and the mean of the projected vertical cross-sectional area ( $A_V$ ) of the particle (Eq. 6):

234

$$235 \quad \Phi_{||} = \frac{\pi D^2}{4(0.5 \times SA - A_V)}$$

Eq. (6)

The crosswise sphericity is the same as the lengthwise sphericity, except for the denominator, which includes the projected horizontal cross-sectional area of the particle ( $A_H$ ), defined as follows:

$$\Phi_{\perp} = \frac{\pi D^2}{4A_H}$$

Eq. (7)

It is noteworthy that the  $V_T$  is required to calculate the  $Re$  and  $V_T$ , which refers to the final product. To solve this problem, the theoretical  $V_T$  (Eq. 2) was used as the input value of Eq. 4 until Eq. 2 converged.

#### **d. Sakurajima volcano**

Japan has around 10% (110) of all of the active volcanos in the world. Sakurajima (1,117m, 31.58° N, 130.65° E, Kyushu, Japan) is an active volcanic island formed around 13,000 years ago, and its tephra is approximately 60–66 %  $SiO_2$  Peléan-type (Oguchi et al., 2009; Takahashi et al., 2013). The major eruptive events in historic age of Sakurajima were 1471–1476 (Bunmei era), 1779–1782 (An-ei era) and 1914 (Taisho era). Sakurajima is an andesitic volcano with two peaks (Kita-dake and Minami-dake). Volcanic activity at Kita-dake ended around 4,900 years ago then it changed to Minami-dake. Activity has centred on Showa crater from 2006 (Iguchi, 2013). Showa crater is located on the eastern flank approximately 500 m east of Minami-dake (Southern Peak) of Sakurajima volcano. It was appeared in 1939 after one month of eruptions that year (Yokoo and Ishihara, 2007). The Minami-dake summit crater was the only active center of Sakurajima volcano until the recommencement of Showa

260 crater from 1948 to 2006. The eruptive activity of Showa crater was resumed in June 2006 and  
261 vulcanian eruptions gradually increased in the autumn of 2009 (Hotta et al., 2016). The Japan  
262 Meteorological Agency (JMA) reported that the eruption frequency of Sakurajima would increase  
263 significantly from 2009 and the accumulated ash fall exceeded  $3.5 \text{ kg m}^{-2}$  in Kagoshima city in 2012.  
264 The Ministry of Land, Infrastructure, Transport, and Tourism (MLITT) installed an operational X-  
265 band radar 10.7 km from the vent, as well as 16 automatic volcanic ash weight measurements, to  
266 observe volcanic eruptions in 2011 (Fig. 3).

267

268

#### 269 **e. Free fall experiments**

270 The data were collected by automatic volcanic ash weight measurements performed on the  
271 Sakurajima volcano (Tajima et al., 2015; Maki et al., 2014; 2016). The free-fall experiments were  
272 divided into two types; one was performed for each phi scale ( $\Phi = -\log_2 D$ ) from  $\Phi = 3$  to  $-4$  ( $0.125 <$   
273  $D < 16 \text{ mm}$ ), and the other was not considered on a particle size scale. The former data, expressed by  
274 A and B (Type 1), were collected at two sites and screened by size (Fig. 4); the latter data, expressed  
275 as C–E (Type 2), were collected at 18 sites (Table 2). Free-fall experiments on collected volcanic ash  
276 particles were carried out in the large-scale rainfall simulator of the National Research Institute for  
277 Earth Science and Disaster Prevention (NIED) in Tsukuba, Japan. The collected particles were dropped  
278 manually around 17 m from the ground and re-collected by a third-generation 2DVD (Maki et al.,  
279 2016). Each sample was dropped for 30 sec to stimulate dispersion, and the measurement period was  
280 1 min. To avoid wind effects including turbulence, the 2DVD was surrounded by a  $3^3$  cubic meter  
281 windbreaking wall (Fig. 5).

282 The free-fall experiments were conducted at intervals of 1 min over 6 h 30 min, as shown in Fig.  
283 6. The number of particles detected by 2DVD was less than 10,000 for 1 min, and the particle size

284 range of Type1 data set was proportional to its phi-scale, since small particles may be contained by  
285 screening.

286 Figure 7 shows the distribution of raw data (the number of data: 274,215) for  $V_T$  and  $\gamma$  with  $D$ .  
287 There were various  $\gamma$  from 0 to 2 when  $D < 2$  mm and most of the data were concentrated near  $\gamma = 0$ .  
288 The  $\gamma$  values converged around 1 and their distributional range decreased with  $D$ . The median value  
289 with a 0.25 mm  $D$  interval corresponded well to the center of the data contour. The median line  
290 converged around  $\gamma = 0.935$  based on the correlation coefficient value (CC). When this was higher  
291 than 0.95 for each  $D$  interval, the data converged. According to this condition, the range of  $2 < D < 5$   
292 mm was satisfied and the mean value was calculated using these data. The  $V_T$  had a wider range when  
293  $D < 2$  mm but the median line corresponded well to the center of the data (Fig. 7b). The line  
294 representing the largest amount of data is lower than the volcanic ash discussed by Bonadonna et al.  
295 (2011). To select a available range of  $D$ , a theoretical terminal velocity equation ( $V_{T,Ref}$ ) for a non-  
296 sphere corresponding to Eqs. 2–7 was used as the reference. The particle density associated with the  
297 eruption of Sakurajima volcano is between 2.43 and 2.59 g cm<sup>-3</sup> (Oguchi et al., 2009), but the actual  
298 particles contain air vacuoles (Van Eaton et al., 2012). This means that  $\rho_s$ , including vacuoles, is  
299 smaller than  $\rho_s$ . Therefore, the minimum  $\rho_s$  was considered to be 2.43 g cm<sup>-3</sup>, and this was used as an  
300 input parameter. The atmospheric conditions of  $T$  and  $P$  were considered from an automatic weather  
301 station (AWS), supported by the JMA. The falling height of a particle which follows the  
302 aforementioned conditions ( $\gamma = 0.935$ ,  $\rho_s = 2.43$  g cm<sup>-3</sup>) when  $D = 4$  was lower than that under the  
303 condition of free fall experiment (17 m) when it reached 90% of  $V_T$  (13.9 m); therefore, the available  
304 data range is considered to be  $D \leq 4$  mm, and this would satisfy the terminal fall velocity. The detailed  
305 equations used in the present study are shown in Appendix A.

306

307

308 **f. Quality control procedures**

309 The 2DVD was originally developed to detect raindrop hydrometeors. For this reason, additional  
310 quality control (QC) checks were deemed necessary to ensure applicability to non-hydrometeors, such  
311 as volcanic ash particles. Specifically, we performed the following three QC procedures for accurate  
312 analysis of the data:

313 i) Particle  $D > 0.25$  mm was selected in consideration of the minimum spatial resolution of 2DVD.

314 ii) If the major axis observed by 2DVD was 10% longer than that of the value calculated directly  
315 based on data coordinates, the data were considered erroneous and thus removed. A 10% bias range  
316 was considered due to mathematical error, the irregular particle shape, and the limitation of the  
317 spatiotemporal resolution of 2DVD.

318 iii) To consider volcanic ash particle, the sample satisfying in the certain range of terminal velocity  
319 relationship was selected. If we consider a single  $V_T$  QC measure for the entire particle shape types, a  
320 number of available data will be removed since  $V_T$  critically depends on particle shape. Therefore, we  
321 applied a 60%  $V_T$  QC threshold (Jaffrain et al., 2011) for each particle shape type. It could be applied  
322 once  $V_T$  relationship of volcanic ash particles is obtained. After selecting the particle shape types and  
323 applying these two QC procedures (i and ii), 19.31% of the data (62,953) remained (Table 1).

324

325

326



327

### 328 **3. Results**

329

#### 330 **a. Ash particle shape**

331 The ash particle size over the entire volcanic ash sample was skewed leftward, and the dominant  
332 particle shape type changed with particle size (Fig. 8). The particles were predominantly horizontally  
333 oriented (75.51%) and vertically oriented (21.60%). Oblate and prolate spheroids made up 76.26% and  
334 23.85% of the particles, respectively. Hence, the particles were mainly OH (57.38%) or PH (15.88%)  
335 (Table 2). The particles were predominantly  $0.25 < D < 0.5$  mm (63.00%) or  $0.5 < D < 1$  mm (32.80%).  
336 Relatively few particles had  $D > 1$  mm (4.20%).

337 There was large variation in shape among particles  $0.25 < D < 0.5$  mm, but the variation decreased  
338 with increasing  $D$ . All of the particle shape types had the largest number of particle at  $D > 1.0$  mm and  
339 the next were shown at  $0.5 < D < 1.0$  mm, except for OH. In total, 95.80% of OH particles had  $D < 1$   
340 mm; at  $D < 0.5$  mm, the value was 75.68%, and at  $D = 0.5-1$  mm, it was 22.36%. In the cases of PH  
341 and OV, 93.63% and 93.87% of these particles, respectively, had  $D < 1$  mm. Beyond  $D > 1$  mm, the  
342 differences in the number of particles for each particle shape type were considerably decreased.

343

344

#### 345 **b. Terminal velocity**

346 The  $V_T$  for the entire particle shape types well follows a polynomial regression analysis which was  
347 applied to define the nonlinear relationship between  $V_T$  and  $D$  (Fig. 9a). It corresponds to that obtained  
348 by Miwa et al (2015), who analyzed Parsivel data using the same laboratory experiments. There was  
349 the inflection point of  $V_T$  at  $D < 1.3$  mm and it came from an increase in the number of OH and an  
350 decrease in their  $V_T$  when  $D < 1$  mm. It can be seen the  $V_T$  relationship for each particle shape type.

351 The observed values of  $V_T$  were well classified by particle shapes (Fig. 9b). The highest values of  
352  $V_T$  were recorded in the order of prolate, sphere, and oblate. Vertically oriented particles had higher  
353  $V_T$  values than horizontal ones. The  $V_T$  for every particle type can be expressed in a power-law form,  
354 except for OH. OH particles followed the regression line relatively closely, and showed the highest  
355 CC and root mean square error (RMSE) values, of 0.94 and 0.46  $\text{m s}^{-1}$ , respectively. Horizontally  
356 orientated particles had relatively higher correlations (OH: 0.94, PH: 0.87) compared to those with a  
357 vertical orientation (OV: 0.75, PV: 0.71). The  $V_T$  relationships and those of statistical parameters are  
358 summarized in Table 3.

359 To verify the reliability of the particle data obtained by 2DVD, which was originally developed to  
360 detect liquid raindrops,  $\rho_s$ ,  $C_D$ , and  $Re$ , as well as theoretical  $V_T$  values according to these parameters,  
361 were analyzed. To calculate the parameters of interest, including the surface area and cross-sectional  
362 area of irregular particles, we applied the irregular particle volume estimation equations of Huang et  
363 al. (2010).

364

365

### 366 **c. Aerodynamic properties**

367 Particle densities were estimated using the  $V_{T,Ref}$ , converged to  $2.37 \text{ g cm}^{-3}$  when  $D < 1.5 \text{ mm}$  (Fig.  
368 10a). This value corresponds well to that of the minimum  $\rho_s$  ( $2.43 \text{ g cm}^{-3}$ ) reported by Oguchi et al.  
369 (2009). The slight difference is likely due to observation errors and the presence of vesicles (e.g.,  
370 Seligman et al., 2016). The median value of  $\rho_s$  is changed to  $0.5 < D < 1.5 \text{ mm}$ , and this range  
371 corresponds to that of  $V_T$ . Horizontally oriented particles (OH and PH) have relatively smaller  $\rho_s$  and  
372 vertically oriented particles (OV and PV) have higher density (Fig. 10b); spheres have particle  
373 densities that accord best with  $D$ . The median  $\rho_s$  values for all particle shapes converged when  $D < 2$   
374 mm, and the converged  $\rho_s$  values ranged from 2.35 to  $2.50 \text{ g cm}^{-3}$ .

375 The  $Re$  and  $C_D$  for the all particle shapes ranged from 10 to 4,000 and 0.6 to 20, respectively (Fig.  
376 11a). Higher values of  $C_D$  were observed when  $\log(Re) < 1.845$  ( $Re < 70$ ); above this threshold,  $C_D$   
377 dramatically decreased. These results were derived according to the number of OH particles, which  
378 mainly had  $D < 0.5$  mm, and had higher  $C_D$  and lower  $Re$ . Particle shape was divided into two types:  
379 OH and others (Fig. 11b). OH particles had higher  $C_D$  compared to the other particle shapes, which in  
380 turn showed few differences among themselves. The OH particles experience strong drag forces under  
381 the same flow conditions, leading to lower  $V_T$ . The differences between OH and other particles  
382 diminished with  $Re < 1,000$ . The other particle shapes had relatively higher  $C_D$  in the range  $10 < Re <$   
383  $3,000$ . Rong et al. (2015) analyzed the relationship between  $Re$  and  $C_D$  for oblate and prolate particles,  
384 and showed that OH particles had higher  $C_D$  compared to the reference line (Clift and Gauven, 1971)  
385 in the range  $0 < Re < 400$ . Each relationship is summarized in Fig. 11.

386

387

#### 388 **d. Axis ratio**

389 The  $\gamma$  of a particle affects the backscattering power of electromagnetic waves, and it is necessary  
390 to calculate the horizontal reflectivity ( $Z$  in dBZ), differential reflectivity ( $Z_{DR}$  in dB), and specific  
391 differential phase shift ( $K_{DP}$  in  $^{\circ} \text{ km}^{-1}$ ). Note that previous studies have analyzed the  $\gamma$  distribution for  
392 raindrops and snow, including hail; however, few studies have been reported on  $\gamma$  of ash particles  
393 compared to those for hydrometeor.

394 Figure 12 shows the quartiles and median values of  $\gamma$  for the entire particle shapes, and for each  
395 individual particle shape type. The  $\gamma$  had a higher standard deviation ( $\sigma_{\gamma}$ ) of  $> 0.25$  when  $D < 0.75$  mm,  
396 which decreased and converged to  $\sigma_{\gamma} = 0.15$  when  $D > 1$  mm (Fig. 12a). The  $\gamma$  in the lower  $\sigma_{\gamma}$  range  
397 converged to  $\gamma = 0.94$  and could be expressed as follows:

398

399 
$$\gamma(D) = 0.94 - 0.25\exp(-1.90 D)$$

400 Eq. (8)

401 The particles are more easily classified by shape than by  $V_T$  (Fig. 12b). Every particle shape type  
402 was independent of  $D$ , except for OH. The  $\gamma$  of each particle types are expressed the following  
403 relationships (Eqs. 9–12):

404  
405 
$$\gamma(D)_{OH} = 0.37 \tanh(1.84D - 1.88) + 0.38$$

406 Eq. (9)

407 
$$\gamma_{OV} = 1.15$$

408 Eq. (10)

409 
$$\gamma_{PH} = 0.88$$

410 Eq. (11)

411 
$$\gamma_{PV} = 1.24$$

412 Eq. (12)

413

414 The parameter  $\gamma(D)_{OH}$  was calculated using the hyperbolic tangent ( $\tanh$ ) for the following reasons:

415 i) its range of values was wider than those of other particle types; ii) the data distribution changed  
416 continuously with  $D$ ; and iii) it was present in a higher proportion (30.44%) compared to the other  
417 parameters. We found that variations in  $\gamma$  decreased with  $D$  and the proportion of Sp shapes increased  
418 when  $D > 2$  mm. The particle types OV and PH showed a wide distribution over  $1 < \gamma < 1.5$  and  $0.4 <$   
419  $\gamma < 1.0$ , respectively, when  $D < 2$  mm, but the variability in median values was relatively low. The  
420 relationships of  $\gamma$  for each particle shape type could be expressed by constant values at  $\gamma = 0.75$  (OH),  
421  $0.88$  (PH),  $1.15$  (OV), and  $1.24$  (PV), respectively, and these differences are around  $\gamma = 0.12$ .

422

423

#### 424 **e. Canting angle**

425 Statistical analysis of  $\beta$  is required to understand the aerodynamic properties of volcanic ash  
426 particles, and the input parameters of T-matrix scattering simulations, to verify the observed radar  
427 variables. The histogram of  $\beta_R$  can be shown in Fig. 13

428 More than 95% of  $\beta$  values for each particle shape type were concentrated in the range  $|\beta_R| \leq 30^\circ$ ,  
429 with  $0^\circ$  as the center (Fig. 13). The particles were symmetrically distributed around  $0^\circ$  and more than  
430 50% were concentrated in the range  $|\beta_R| < 4^\circ$ . The horizontally oriented  $\beta$  distribution was relatively  
431 narrow ( $|\beta_R| < 20^\circ$ ) and exhibited a unimodal distribution. It is noteworthy that 90% of OH particles  
432 were concentrated in the range  $|\beta_R| < 4^\circ$ . The vertically oriented  $\beta$  distribution was relatively broader  
433 ( $|\beta_R| < 30^\circ$ ) and followed a bimodal distribution. PV exhibited a bimodal form, but this was not  
434 symmetrical about  $0^\circ$ . For spheres, the  $\beta$  distribution was narrower, similar to horizontally oriented  
435 particles, and it had a bimodal distribution, similar to vertically oriented particles, indicating that the  
436 independent features of both orientations were combined.

437 The values of  $|\overline{\beta_R}|$  and  $|\sigma_\beta|$  for OH and PV (OV, PH) were  $0^\circ$  and  $3.5^\circ$  ( $0.4^\circ$ ,  $13.1^\circ$ ), and  $1.3^\circ$  and  
438  $12.7^\circ$  ( $0.2^\circ$ ,  $10.9^\circ$ ), respectively. OV (OH) had the highest (lowest) value of  $|\sigma_\beta|$ . This validates the  
439 assumption of Marzano et al. (2012) under stable conditions ( $|\sigma_\beta| = 10^\circ$ ). Therefore, we believe that  
440 the tumbling phenomenon ( $|\sigma_\beta| > 30^\circ$ ) of the particles under calm atmospheric conditions was likely to  
441 be minor.

442 To analyze the correlation between particle D and  $\beta$ , quartiles for each particle D interval were  
443 calculated (Fig. 14). The particles were concentrated at  $|\beta_R| < 30^\circ$  regardless of D, and median values  
444 were stable when  $D < 1$  mm for the entire particle shape types; however, fluctuation increased with D  
445 (Fig. 14a). The  $|\sigma_\beta|$  values gradually increased from  $10^\circ$  to  $13^\circ$  when  $0.3 < D < 1.3$  mm and variability  
446 was greatest around the center ( $13^\circ$ ). This increase in  $|\sigma_\beta|$  would not be expected in the case of a

447 relatively small number of particles (Fig. 8a), since their standard deviation is largely maintained at  
448 about  $13^\circ$  regardless of dataset size.

449 Variability in the median values for individual particles was more apparent. The values converged  
450 around  $0^\circ$  but fluctuation increased with greater  $D$  from the zero line. The median  $|\beta_R|$  values  
451 exceeded  $3^\circ$ ,  $5^\circ$ ,  $10^\circ$ , and  $15^\circ$  when  $D > 1$  mm,  $1 < D < 2$  mm,  $2 < D < 3$  mm, and  $D > 3$  mm,  
452 respectively (Fig. 14b).

453

#### 4. Discussions

The results of present study can be extended in viewpoint of the radar meteorology: i) the radar observation and ii) ashfall rate ( $R_A$ ) estimations. i) Weather radar operates for a similar purpose to that of meteorological satellites, and provides information for determining the volume, mass, and echo top height of weather systems. Short-duration eruptions, i.e., less than 1 hour, can be detected at high spatio-temporal resolution, especially in the early period of an eruption. The temporal resolution of weather radar is a few minutes for a single volume scan, and depends on the observation strategy and radar band. The spatial resolution of weather radar is a few hundred meters and is proportional to the radar frequency. A number of ash cloud detections were reported in several observational cases in the US and Japan (Maki and Doviak, 2001; Maki et al., 2012). Marzano et al. (2013) summarized 28 major explosive volcanic eruptions detected by weather radars from 1970 to 2011. Harris and Rose (1983) attempted to analyze volcanic ash particle size and total mass using a C-band weather radar. Maki and Doviak (2001) proposed the method to retrieve PSD from radar measurements of volcanic ash and Donnadieu et al. (2012) detected volcanic eruptions using an L-band fixed radar. Marzano et al. (2006, 2012) and Maki et al. (2012, 2014) detected and analyzed volcanic eruptions using weather radars, from theoretical (physical) and experimental (engineering) perspectives. Thus, observability of volcanic ash clouds using weather radar can be confirmed from previous researches. To verify radar-based volcanic ash cloud observations, a scattering simulation can be considered. The basic parameters: axis ratio, canting angle which are the results presented in this study are the input information of scattering simulation to simulate the theoretical radar variables. In particular, the T-matrix scattering simulation developed by Waterman (1965) is useful for calculation of the theoretical backscattering power of non-spherical particles.

Seconds, the  $V_T$  is one of the main parameters for  $R_A$  ( $\text{kg m}^{-2} \text{hr}^{-1}$ ) and it is defined in terms of PSD and  $V_T$  as follows:

478

479

$$R_A = V_r \frac{3.6}{10^3} \int_{D_1}^{D_2} V_T(D) N(D) D^3 dD$$

480

Eq. (13)

481

482

where  $V_r$  is the particle volume ratio. In case of sphere, it is considered as  $\pi/6$ .

483

484

485

486

487

488

489

490

Marzano et al. (2012b) proposed Z- $C_A$  relationships using the ashfall concentration ( $C_A$  in  $\text{g m}^{-3}$ ) and z. Maki et al. (2016) introduced  $R_A$ -z relationship for Sakurajima eruption case (18. Aug. 2013) using the time integration of  $R_A$  ( $S_A$  in  $\text{kg m}^{-2}$ ) obtained by automatic volcanic ash weight measurements. However, once we use the disdrometer such as 2DVD, it will be possible to estimate  $R_A$  directly since 2DVD can measure PSD,  $V_T$  and  $\gamma$ . Therefore, basic parameters could help to simulate radar variables and estimate  $R_A$  which are necessary to develop the quantitative ash fall estimation (QAE) method.



## 491 **5. Summary and Conclusions**

492 The basic parameters ( $V_T$ ,  $\gamma$  and  $\beta$ ) of volcanic ash particles were analyzed from the free fall  
493 experiments with 2DVD. Data were collected with 18 automatic volcanic ash weight measurements  
494 performed on Sakurajima volcano, Japan (31.58° N, 130.65° E). To identify the aerodynamic properties  
495 of the volcanic ash particles in the samples, a free-fall experiment was conducted in the large-scale  
496 rainfall simulator of the NIED, and 274,215 samples were analyzed.

497 Radar variables are highly dependent on the  $|K|^2$ , size, and shape of particles. Particle types with  
498 rotating symmetric axes were assumed to represent volcanic ash particles which have a wide variety  
499 of irregular shape. Their orientation was also considered with respect to horizontally (OH, PH) and  
500 vertically (OV, PV) oriented oblate and prolate spheroids were studied, respectively.

501 The dominant particle shape comprised horizontally and vertical oriented particles, present in  
502 proportions of 75.51% and 21.60%, respectively. Regarding particle shape, oblate (prolate) spheroids  
503 comprised 76.26% (23.85%) of all particles in the samples. The most common particle shape type was  
504 OH, accounting for 59% of all particles when  $D < 1$  mm, and 69% when  $D < 0.5$  mm. Overall, 95.80%,  
505 93.87%, and 93.63% of the OH, OV, and PH particles had  $D < 1$  mm, respectively.

506 The  $V_T$  of the particles were classified in the order of PV, OV, Sp, PH and OH. These results are  
507 consistent with the  $V_{T, Ref}$ , which suggests that 2DVD is a reliable for observing volcanic ash particles  
508 under stable weather conditions. A noticeable increase in  $V_T$  for OH in the range  $0.5 < D < 1$  mm  
509 occurred through an increase in  $\gamma$ ; this was not observed for other particle types.

510 The estimated  $\rho_s$  converged to  $2.37\text{g cm}^{-3}$  when  $D > 1.5$  mm, and the median value changed over  
511 the range  $0.5 < D < 1.5$  mm. The converged value of  $\rho_s$  is consistent with the value for the Sakurajima  
512 volcano reported by Oguchi et al. (2009). The relationship of  $C_D$  and  $Re$  were divided into two particle  
513 type categories (OH and the others) and  $C_D(\text{OH})$  was dramatically increased in the range of  $Re < 70$ .  
514 These results were derived from the particle concentration of OH, which was highest when  $D < 0.5$

515 mm; at this threshold,  $C_D$  was higher and  $Re$  was lower. The range of  $V_T$  over  $0.7 < D < 1.3$  mm was  
516 informed by both  $\gamma$  and  $\rho_s$ .

517 The  $\sigma_\gamma$  decreased in the range of  $D > 0.75$  mm, to 0.15, and converged to  $\gamma = 0.94$ . Maki et al.  
518 (2014) introduced the radar variables and found that  $Z_{DR}$  gradually increased with time; the dominant  
519 values at 10 and 18 min after the eruption were close to 1 and 2 dB, respectively. The results presented  
520 in this study corresponded to volcanic eruption clouds with positive  $Z_{DR}$  since it is a function of  $|K|^2$   
521 and  $\gamma$  (Herzogh and Jameson, 1992). In addition, it can be explained that the size sorting of ash particle  
522 (e.g., Beckett et al., 2015; Stevenson et al., 2015) will affect the increase of  $Z_{DR}$  by the results of  
523 present study.

524 The  $|\sigma_\beta|$  of OV particles with  $|\beta_0| = 90^\circ$  was largest ( $13.1^\circ$ ) among all particle types and OH particles  
525 had the lowest  $|\sigma_\beta|$  at  $3.5^\circ$ . Based on the  $|\sigma_\beta|$  results, the tumbling phenomenon would not be dominant  
526 under calm atmospheric conditions. The quartiles were stable when  $D < 1$  mm for the entire particle  
527 shape types, but increased with  $D$ . The value of  $\sigma_\beta$  was higher when  $D < 1.3$  mm and started to converge  
528 around  $13^\circ$  due to a decrease in the number of OH particles.

529 These results could be the essential information to develop the new approaches for detecting non-  
530 hydrometeors and numerical model. The axis ratio and canting angle of ash particles obtained from  
531 the present study are necessary for scattering simulations.  $V_T$  obtained by the present study suggests  
532 that smaller particles can be transported longer distance. Therefore, it will be useful for scattering  
533 simulation of ash particles to develop QAE and help to improve a numerical model using  $V_T$  obtained  
534 by the present study.

535

536

### **Author contributions**

537

Masato Iguchi and Masayuki Maki designed the study. Akihiko Yamaji and Tatsuya Momotani

538

collected the samples and performed the free-fall experiment. Sung-Ho Suh modified the original study

539

theme and performed the study. Masayuki Maki and Sung-Ho Suh performed research, obtained the

540

results and prepared the manuscript along with contributions from all of the co-authors. Dong-In Lee

541

examined the results and checked the manuscript.

542

543

### **Acknowledgments**

544

This work was supported by a Grant-in Aid for JSPS KAKENHI (grant number JP16H03145) and

545

partially supported by a DPRI collaborative research grant (Kyoto Univ. 25G-11). The authors

546

acknowledge the provision of ashfall data and funding for this work from Kyoto and Kagoshima

547

Universities. The 2DVD data were provided by MEXT, Japan. We also thank the NIED for use of

548

their large-rainfall simulator.

549

550 **Appendix A**

551

552 The theoretical fall velocity and falling distance with time are calculated as follows;

553

554

$$F = ma = F_g - F_D$$

555

Eq. (A1)

556

$$F_g = mg$$

557

Eq. (A2)

558

$$F_D = \frac{1}{2} \rho_g V^2 C_D A$$

559

Eq. (A3)

560

561 where  $F_g$  is universal gravitation,  $F_D$  is drag force,  $m$  is mass, and  $a$  is the free-fall acceleration.

562 In Eq. A2,  $g$  is the acceleration due to gravity, considered to be  $9.81 \text{ m s}^{-2}$ , and  $V$  and  $C_D$  in Eq. A3

563 correspond to the values in Eq. 2–7. The symbols  $\mu$  and  $\rho_g$  are the dynamic viscosity and density of

564 the atmosphere and were assumed as  $1.837 \times 10^{-5} \text{ kg m}^{-1} \text{ s}^{-1}$  and  $1.194 \times 10^{-5} \text{ g cm}^{-3}$ , respectively.

565 The results were based on conditions at an atmospheric  $T$  as  $25 \text{ }^\circ\text{C}$ .

566 To ensure accuracy, we considered the surface roughness effect of a volcanic ash particle ( $1.07^{-1}$ )

567 on the fall velocity, as suggested by Bagheri and Bonadonna (2016), and the results for  $D = 4 \text{ mm}$

568 are shown in Fig. A1.

569 **References**

- 570 Böhm, H. P.: A general equation for the terminal fall speed of solid hydrometeors, *Journal of the*  
571 *Atmospheric Sciences*, 46, 2419-2427, 1989.
- 572 Bagheri, G., Bonadonna, C., Manzella, I., Pontelandolfo, P., and Haas, P.: Dedicated vertical wind  
573 tunnel for the study of sedimentation of non-spherical particles, *Review of Scientific*  
574 *Instruments*, 84, 054501, 2013.
- 575 Bagheri, G. and Bonadonna, C.: On the drag of freely falling non-spherical particles, *Powder*  
576 *Technology*, 301, 526-544, 2016.
- 577 Beckett, F., Witham, C., Hort, M., Stevenson, J., Bonadonna, C., and Millington, S.: Sensitivity of  
578 dispersion model forecasts of volcanic ash clouds to the physical characteristics of the  
579 particles, *Journal of Geophysical Research: Atmospheres*, 120, 2015.
- 580 Bonadonna, C., Ernst, G., and Sparks, R.: Thickness variations and volume estimates of tephra fall  
581 deposits: the importance of particle Reynolds number, *Journal of Volcanology and*  
582 *Geothermal Research*, 81, 173-187, 1998.
- 583 Bonadonna, C., Genco, R., Gouhier, M., Pistolesi, M., Cioni, R., Alfano, F., Hoskuldsson, A., and  
584 Ripepe, M.: Tephra sedimentation during the 2010 Eyjafjallajökull eruption (Iceland)  
585 from deposit, radar, and satellite observations, *Journal of Geophysical Research: Solid*  
586 *Earth (1978–2012)*, 116, 2011.
- 587 Bonadonna, C., Folch, A., Loughlin, S., and Puempel, H.: Future developments in modelling and  
588 monitoring of volcanic ash clouds: outcomes from the first IAVCEI-WMO workshop on  
589 Ash Dispersal Forecast and Civil Aviation, *Bulletin of volcanology*, 74, 1-10, 2012.

590 Clift, R. and Gauvin, W.: Motion of particles in turbulent gas streams, *British Chemical Engineering*,  
591 16, 229-236, 1971.

592 Coltelli, M., Miraglia, L., and Scollo, S.: Characterization of shape and terminal velocity of tephra  
593 particles erupted during the 2002 eruption of Etna volcano, Italy, *Bulletin of volcanology*,  
594 70, 1103-1112, 2008.

595 Del Bello, E., Taddeucci, J., Vitturi, M. d. M., Scarlato, P., Andronico, D., Scollo, S., Kueppers, U.,  
596 and Ricci, T.: Effect of particle volume fraction on the settling velocity of volcanic ash  
597 particles: insights from joint experimental and numerical simulations, *Scientific reports*,  
598 7, 39620, 2017.

599 Dellino, P., Mele, D., Bonasia, R., Braia, G., La Volpe, L., and Sulpizio, R.: The analysis of the  
600 influence of pumice shape on its terminal velocity, *Geophysical Research Letters*, 32,  
601 2005.

602 Dioguardi, F., Mele, D., Dellino, P., and Dürig, T.: The terminal velocity of volcanic particles with  
603 shape obtained from 3D X-ray microtomography, *Journal of Volcanology and Geothermal*  
604 *Research*, 329, 41-53, 2017.

605 Dioguardi, F., Mele, D., and Dellino, P.: A New One-Equation Model of Fluid Drag for Irregularly  
606 Shaped Particles Valid Over a Wide Range of Reynolds Number, *Journal of Geophysical*  
607 *Research: Solid Earth*, 123, 144-156, 2018.

608 Donnadieu, F.: *Volcanological applications of Doppler radars: A review and examples from a*  
609 *transportable pulse radar in L-band*, INTECH Open Access Publisher, 2012.

610 Folch, A., Costa, A., and Macedonio, G.: FALL3D: A computational model for transport and  
611 deposition of volcanic ash, *Computers & Geosciences*, 35, 1334-1342, 2009.

612 Ganser, G. H.: A rational approach to drag prediction of spherical and nonspherical particles, Powder  
613 Technology, 77, 143-152, 1993.

614 Garboczi, E. and Bullard, J.: 3D analytical mathematical models of random star-shape particles via a  
615 combination of X-ray computed microtomography and spherical harmonic analysis,  
616 Advanced Powder Technology, 28, 325-339, 2017.

617 Hölzer, A. and Sommerfeld, M.: New simple correlation formula for the drag coefficient of non-  
618 spherical particles, Powder Technology, 184, 361-365, 2008.

619 Haider, A. and Levenspiel, O.: Drag coefficient and terminal velocity of spherical and nonspherical  
620 particles, Powder technology, 58, 63-70, 1989.

621 Happel, J. and Brenner, H.: Low Reynolds number hydrodynamics: with special applications to  
622 particulate media, Springer Science & Business Media, 2012.

623 Harris, D. M. and Rose, W. I.: Estimating particle sizes, concentrations, and total mass of ash in  
624 volcanic clouds using weather radar, Journal of Geophysical Research: Oceans (1978–  
625 2012), 88, 10969-10983, 1983.

626 Herzegh, P. H. and Jameson, A. R.: Observing precipitation through dual-polarization radar  
627 measurements, Bulletin of the American Meteorological Society, 73, 1365-1376, 1992.

628 Hotta, K., Iguchi, M., and Tameguri, T.: Rapid dike intrusion into Sakurajima volcano on August 15,  
629 2015, as detected by multi-parameter ground deformation observations, Earth, Planets and  
630 Space, 68, 68, 2016.

631 Huang, G.-J., Bringi, V., Cifelli, R., Hudak, D., and Petersen, W.: A methodology to derive radar  
632 reflectivity-liquid equivalent snow rate relations using C-band radar and a 2D video  
633 disdrometer, Journal of Atmospheric and Oceanic Technology, 27, 637-651, 2010.

- 634 Huang, G.-J., Bringi, V., Moisseev, D., Petersen, W. A., Bliven, L., and Hudak, D.: Use of 2D-video  
635 disdrometer to derive mean density–size and Z e–SR relations: Four snow cases from the  
636 light precipitation validation experiment, *Atmospheric Research*, 153, 34-48, 2015.
- 637 Iguchi, M.: Magma Movement from the Deep to Shallow Sakurajima Volcano as Revealed by  
638 Geophysical Observations (< Special Section> Sakurajima Special Issue), *Bulletin of the*  
639 *Volcanological Society of Japan*, 58, 1-18, 2013.
- 640 Jaffrain, J., Studzinski, A., and Berne, A.: A network of disdrometers to quantify the small-scale  
641 variability of the raindrop size distribution, *Water Resources Research*, 47, 2011.
- 642 Joss, J., and Waldvogel A.: A spectrograph for the automatic analysis of raindrops, *Pure and Applied*  
643 *Geophysics*, 69, 240-246, 1967.
- 644 Kruger, A. and Krajewski, W. F.: Two-dimensional video disdrometer: A description, *Journal of*  
645 *Atmospheric and Oceanic Technology*, 19, 602-617, 2002.
- 646 Kunii, D.: 0. Levenspiel, *Fluidization Engineering*, John Wiley, 8, 44-45, 1969.
- 647 Langmann, B., Folch, A., Hensch, M., and Matthias, V.: Volcanic ash over Europe during the eruption  
648 of Eyjafjallajökull on Iceland, April–May 2010, *Atmospheric Environment*, 48, 1-8, 2012.
- 649 Löffler-Mang, M. and Joss. J: An optical disdrometer for measuring size and velocity of hydrometeors,  
650 *Journal of Atmospheric and Oceanic Technology*, 17, 130-139, 2000.
- 651 Maki, M. and Doviak, R.: Volcanic ash size distribution determined by weather radar, 1810-1811,  
652 2001.
- 653 Maki, M., Maesaka, T., Kozono, T., Nagai, M., Furukawa, R., Nakada, S., Koshida, T., and Takenaka,  
654 H.: Quantitative volcanic ash estimation by operational polarimetric weather radar, 2012.



- 655 Maki, M., Maesaka, T., Muraji, Y., and Suzuki, I.: Statistical analysis of volcanic ash measured by X-  
656 band polarimetric radar, 2014.
- 657 Maki, M., Iguchi, M., Maesaka, T., Miwa, T., Tanada, T., Kozono, T., Momotani, T., Yamaji, A., and  
658 Kakimoto, I.: Preliminary results of weather radar observations of sakurajima volcanic  
659 smoke, *Journal of Disaster Research*, 11, 15-30, 2016.
- 660 Marzano, F. S., Barbieri, S., Vulpiani, G., and Rose, W. I.: Volcanic ash cloud retrieval by ground-  
661 based microwave weather radar, *IEEE transactions on geoscience and remote sensing*, 44,  
662 3235-3246, 2006.
- 663 Marzano, F. S., Picciotti, E., Vulpiani, G., and Montopoli, M.: Synthetic signatures of volcanic ash  
664 cloud particles from X-band dual-polarization radar, *IEEE Transactions on Geoscience  
665 and Remote Sensing*, 50, 193-211, 2012.
- 666 Marzano, F. S., Picciotti, E., Montopoli, M., and Vulpiani, G.: Inside volcanic clouds: Remote sensing  
667 of ash plumes using microwave weather radars, *Bulletin of the American Meteorological  
668 Society*, 94, 1567-1586, 2013.
- 669 Nešpor, V., Krajewski, W. F., and Kruger, A.: Wind-induced error of raindrop size distribution  
670 measurement using a two-dimensional video disdrometer, *Journal of Atmospheric and  
671 Oceanic Technology*, 17, 1483-1492, 2000.
- 672 Oguchi, T., Udagawa, M., Nanba, N., Maki, M., and Ishimine, Y.: Measurements of dielectric constant  
673 of volcanic ash erupted from five volcanoes in Japan, *IEEE Transactions on Geoscience  
674 and Remote Sensing*, 47, 1089-1096, 2009.

- 675 Poulidis, A. P., Takemi, T., Iguchi, M., and Renfrew, I. A.: Orographic effects on the transport and  
676 deposition of volcanic ash: A case study of Mount Sakurajima, Japan, *Journal of*  
677 *Geophysical Research: Atmospheres*, 122, 9332-9350, 2017.
- 678 Rong, L., Zhou, Z., and Yu, A.: Lattice–Boltzmann simulation of fluid flow through packed beds of  
679 uniform ellipsoids, *Powder Technology*, 285, 146-156, 2015.
- 680 Rosenfeld, D. and Ulbrich, C. W.: Cloud microphysical properties, processes, and rainfall estimation  
681 opportunities. In: *Radar and Atmospheric Science: A Collection of Essays in Honor of*  
682 *David Atlas*, Springer, 2003.
- 683 Seligman, A. N., Bindeman, I. N., Watkins, J. M., and Ross, A. M.: Water in volcanic glass: From  
684 volcanic degassing to secondary hydration, *Geochimica et Cosmochimica Acta*, 191, 216-  
685 238, 2016.
- 686 Sheppard, B. E.: Measurement of raindrop size distributions using a small Doppler radar, *Journal of*  
687 *Atmospheric and Oceanic Technology*, 7, 255-268, 1990.
- 688 Sigurdsson, H., Houghton, B., McNutt, S., Rymer, H., and Stix, J.: *The encyclopedia of volcanoes*,  
689 Elsevier, 2015.
- 690 Stevenson, J., Millington, S., Beckett, F., Swindles, G., and Thordarson, T.: Big grains go far:  
691 understanding the discrepancy between tephrochronology and satellite infrared  
692 measurements of volcanic ash, *Atmospheric Measurement Techniques*, 8, 2069-2091,  
693 2015.
- 694 Stokes, G. G.: *On the effect of the internal friction of fluids on the motion of pendulums*, Pitt Press  
695 Cambridge, 1851.

696 Suzuki, T.: A theoretical model for dispersion of tephra, *Arc volcanism: physics and tectonics*, 95, 113,  
697 1983.

698 Takahashi, M., Otsuka, T., Sako, H., Kawamata, H., Yasui, M., Kanamaru, T., Otsuki, M., Kobayashi,  
699 T., Ishihara, K., and Miki, D.: Temporal Variation for Magmatic Chemistry of the  
700 Sakurajima Volcano and Aira Caldera Region, Southern Kyushu, Southwest Japan since  
701 61 ka and Its Implications for the Evolution of Magma Chamber System, *Bulletin of the*  
702 *Volcanological Society of Japan*, 58, 19-42, 2013.

703 Tajima, Y., Ohara, D., Fukuda, K., and Shimomura, S.: Development of Automatic Tephrometer for  
704 Monitoring of Volcano, 39-46, 2015.

705 Thurai, M. and Bringi, V.: Drop axis ratios from a 2D video disdrometer, *Journal of Atmospheric and*  
706 *Oceanic Technology*, 22, 966-978, 2005.

707 Tokay, A., Wolff, D. B., and Petersen, W. A.: Evaluation of the new version of the laser-optical  
708 disdrometer, OTT Parsivel2, *Journal of Atmospheric and Oceanic Technology*, 31, 1276-  
709 1288, 2014.

710 Tran-Cong, S., Gay, M., and Michaelides, E. E.: Drag coefficients of irregularly shaped particles,  
711 *Powder Technology*, 139, 21-32, 2004.

712 Van Eaton, A. R., Muirhead, J. D., Wilson, C. J., and Cimarelli, C.: Growth of volcanic ash aggregates  
713 in the presence of liquid water and ice: an experimental approach, *Bulletin of volcanology*,  
714 74, 1963-1984, 2012.

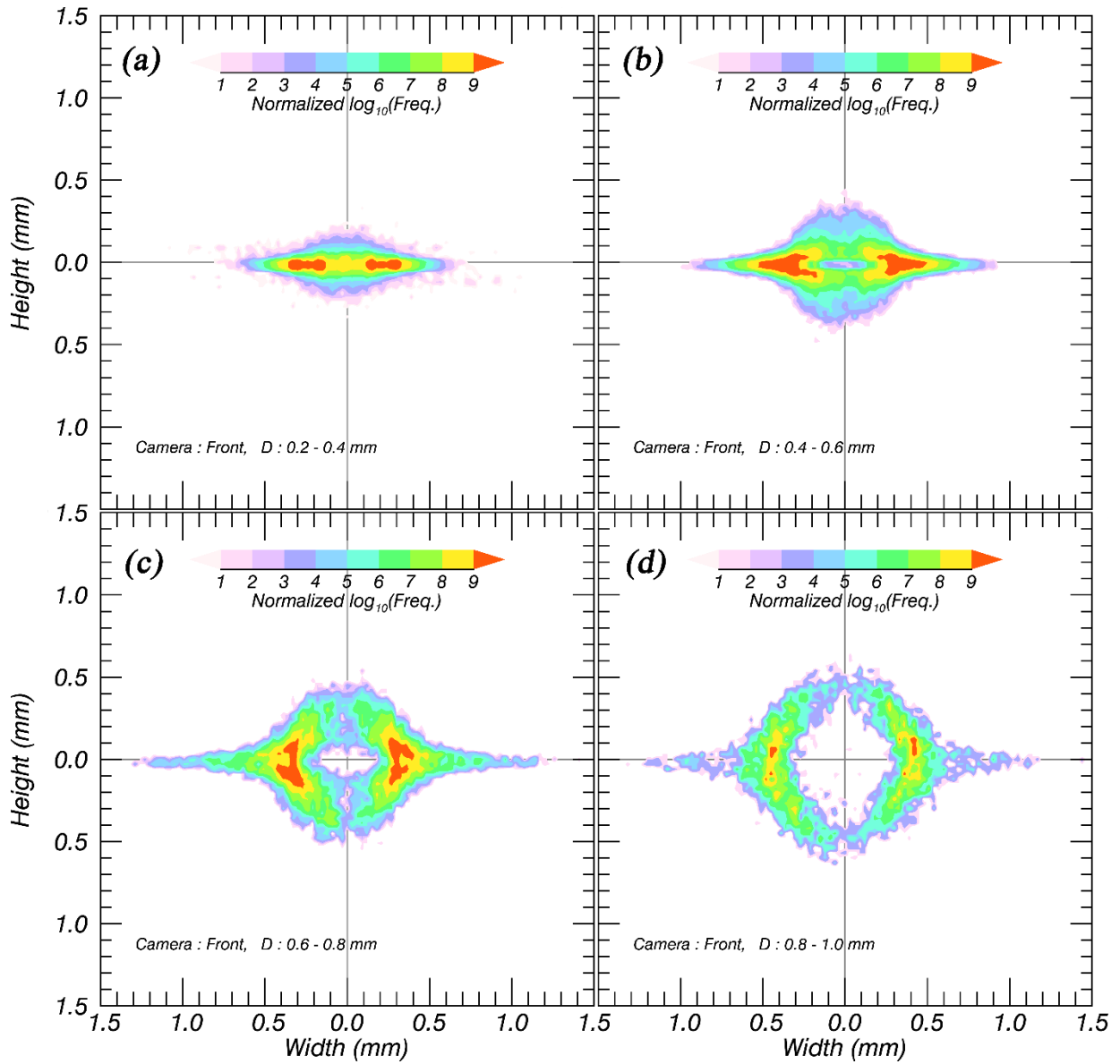
715 Waterman, P. C.: Symmetry, unitarity, and geometry in electromagnetic scattering, *Physical review D*,  
716 3, 825, 1971.

- 717 Wilson, L. and Huang, T.: The influence of shape on the atmospheric settling velocity of volcanic ash  
718 particles, *Earth and Planetary Science Letters*, 44, 311-324, 1979.
- 719 Wilson, T. M., Stewart, C., Sword-Daniels, V., Leonard, G. S., Johnston, D. M., Cole, J. W., Wardman,  
720 J., Wilson, G., and Barnard, S. T.: Volcanic ash impacts on critical infrastructure, *Physics  
721 and Chemistry of the Earth, Parts A/B/C*, 45, 5-23, 2012.
- 722 Wilson, T. M., Jenkins, S., and Stewart, C.: Impacts from volcanic ash fall. In: *Volcanic Hazards,  
723 Risks and Disasters*, Elsevier, 2015.
- 724 Yokoo, A. and Ishihara, K.: Volcanic activity around Showa Crater of Sakurajima Volcano monitored  
725 with infrared and video cameras, *Annals of Disas. Prev. Res. Inst., Kyoto Univ.*, No. 50  
726 C., 2007.
- 727
- 728

729

# Figures

730



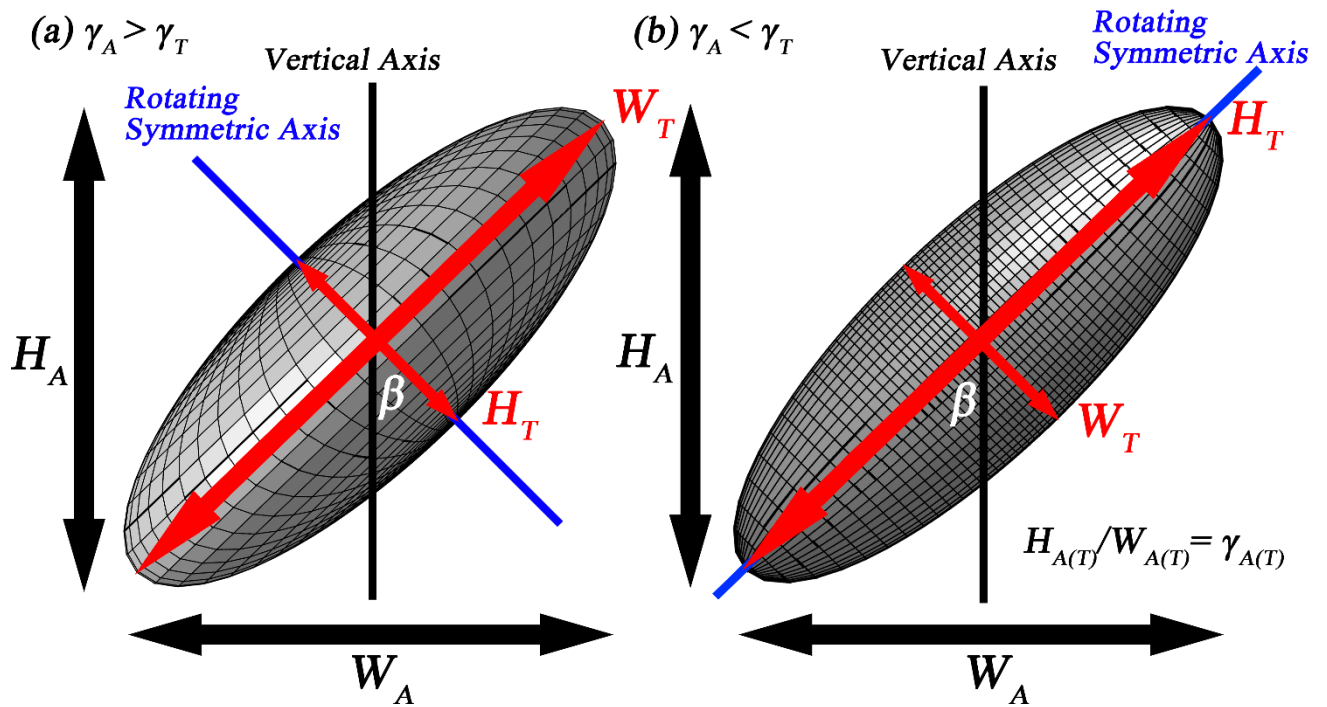
731

732 Figure 1. Accumulated contoured images of volcanic ash particles with D measured by a two-  
733 dimensional video disdrometer (2DVD).

734

735

736



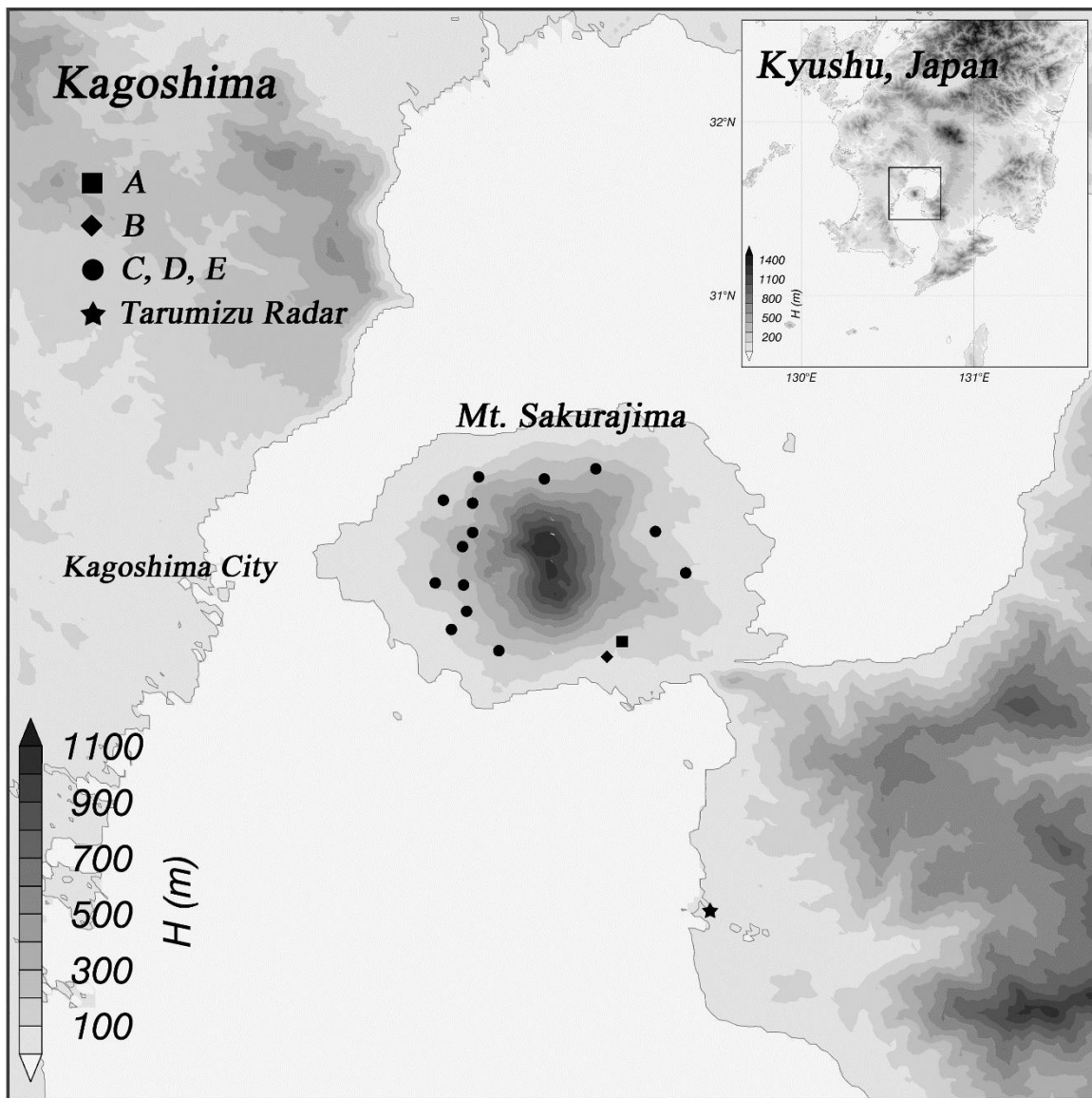
737

738 Figure 2. Conceptual model of an (a) oblate and (b) prolate spheroid with the same canting angle  
 739 ( $\beta$ ).  $W_{A(T)}$  and  $H_{A(T)}$  are the apparent (true) width and height of the particle, respectively.  $\gamma_{A(T)}$  is the  
 740 apparent (true) axis ratio.

741

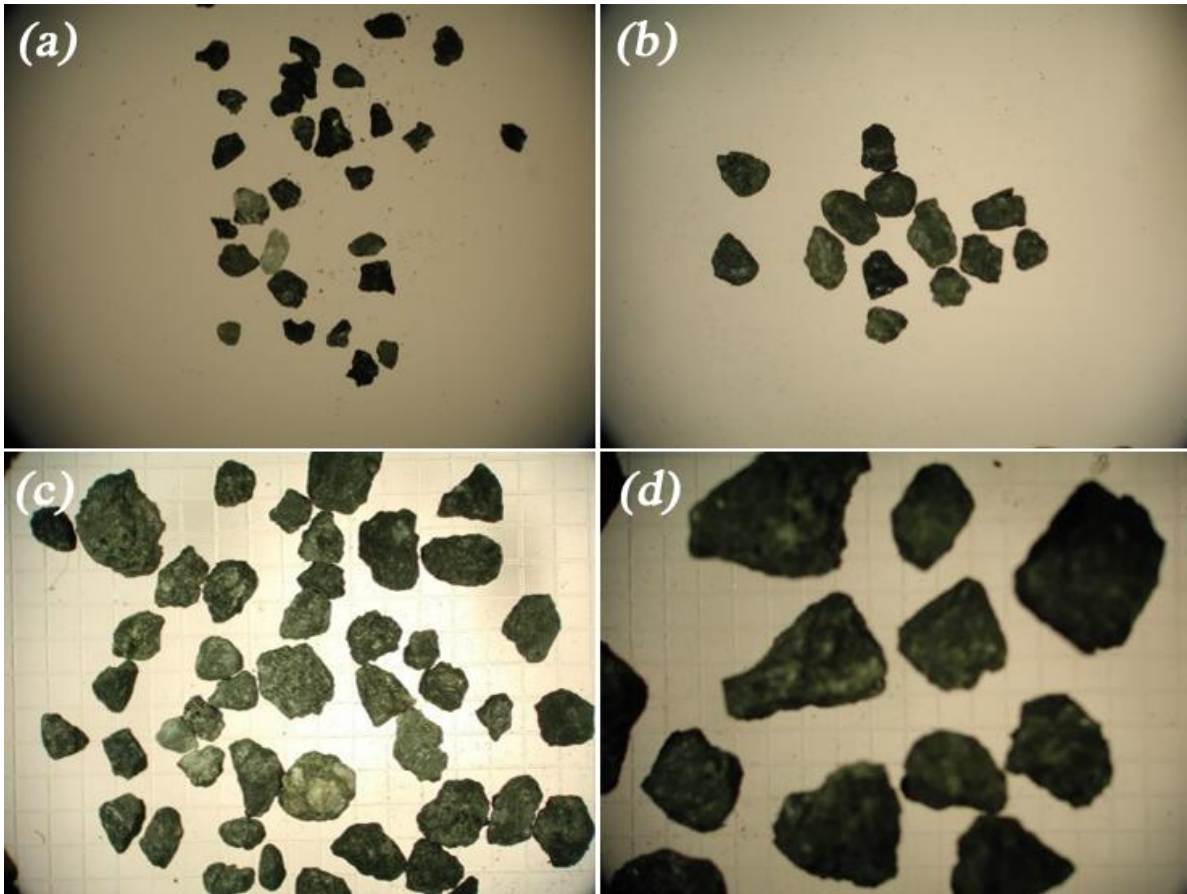
742

743



744  
 745  
 746  
 747  
 748  
 749  
 750

Figure 3. The locations of tephrometers and Showa crater on Sakurajima volcano, Japan. Black symbols indicate the locations of tephrometers and the star, square, and circle symbols correspond to datasets A, B and C–E, respectively. The white circle symbol represents the location of Showa crater.



751

752

753

754

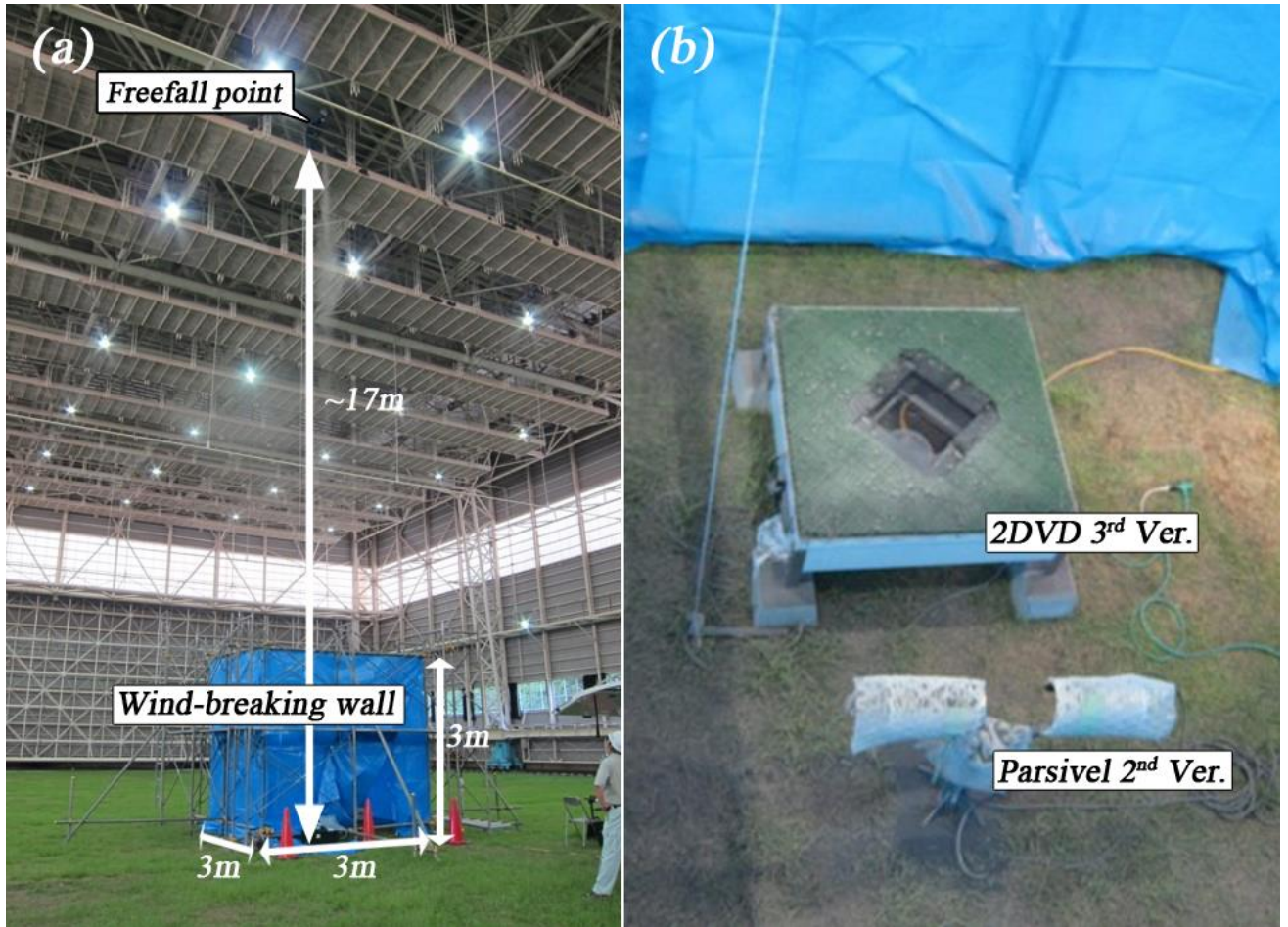
755

756

757

Figure 4. Real images of volcanic ash particles used in the present study. The particles were classified as (a)  $0.125 \text{ mm} < D \leq 0.25 \text{ mm}$ , (b)  $0.25 \text{ mm} < D \leq 1 \text{ mm}$ , (c)  $1 \text{ mm} < D < 2 \text{ mm}$ , and (d)  $2 < D \leq 4 \text{ mm}$ .





758

759

760

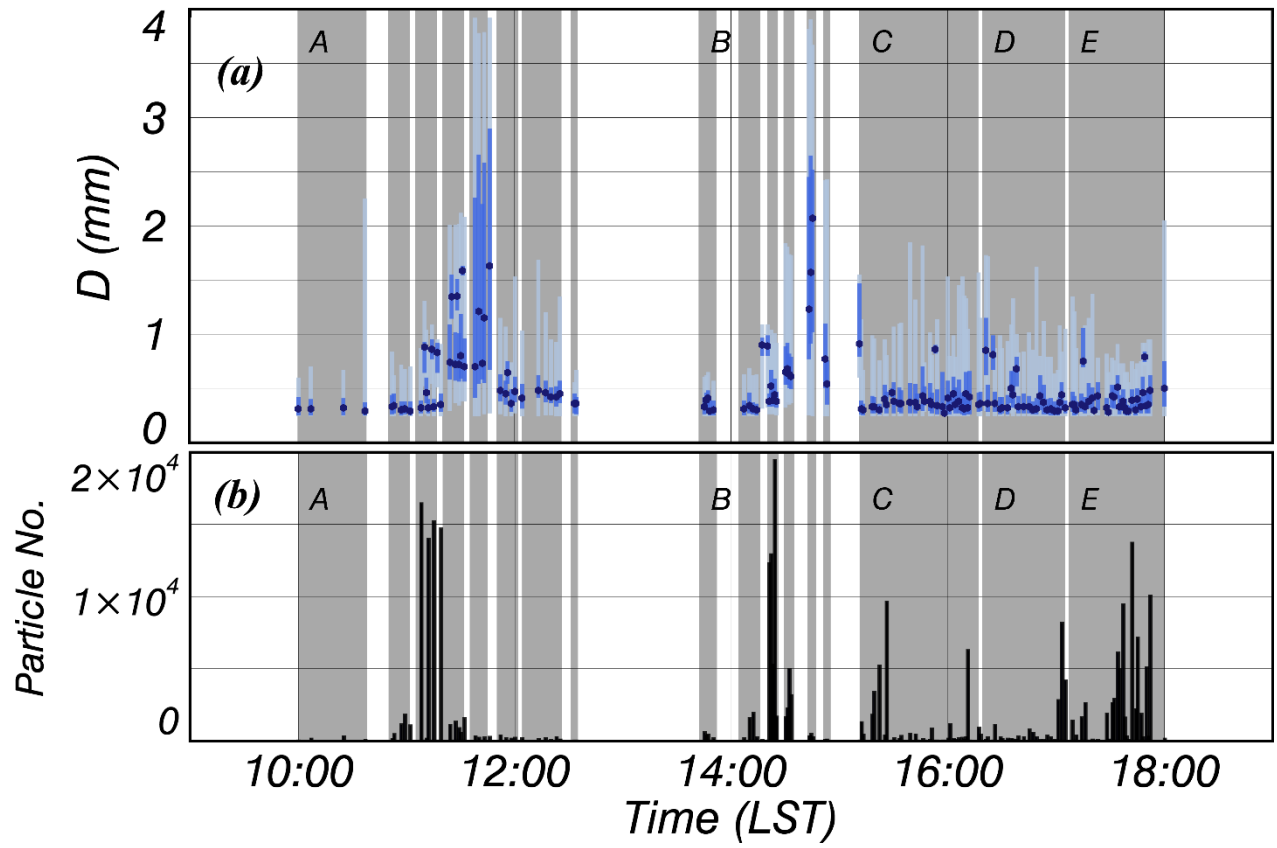
761

762

763

764

Figure 5. Free-fall experiment conditions of volcanic ash particles on the (a) outside and (b) inside of the wind-breaking wall covering the disdrometers in the large-scale rainfall simulator of the National Research Institute for Earth Science and Disaster Prevention (NIED).



765

766

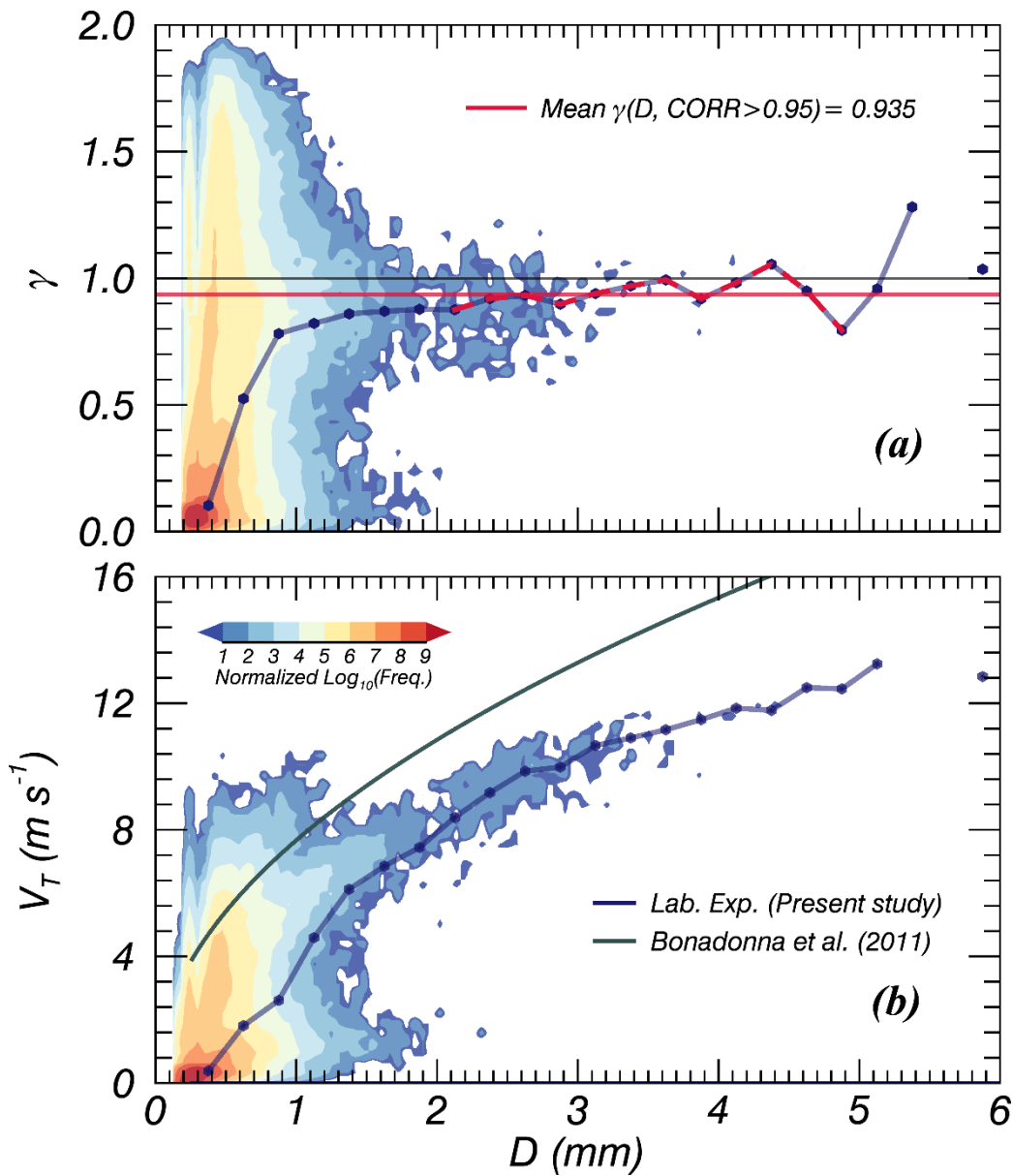
767

768

769

770

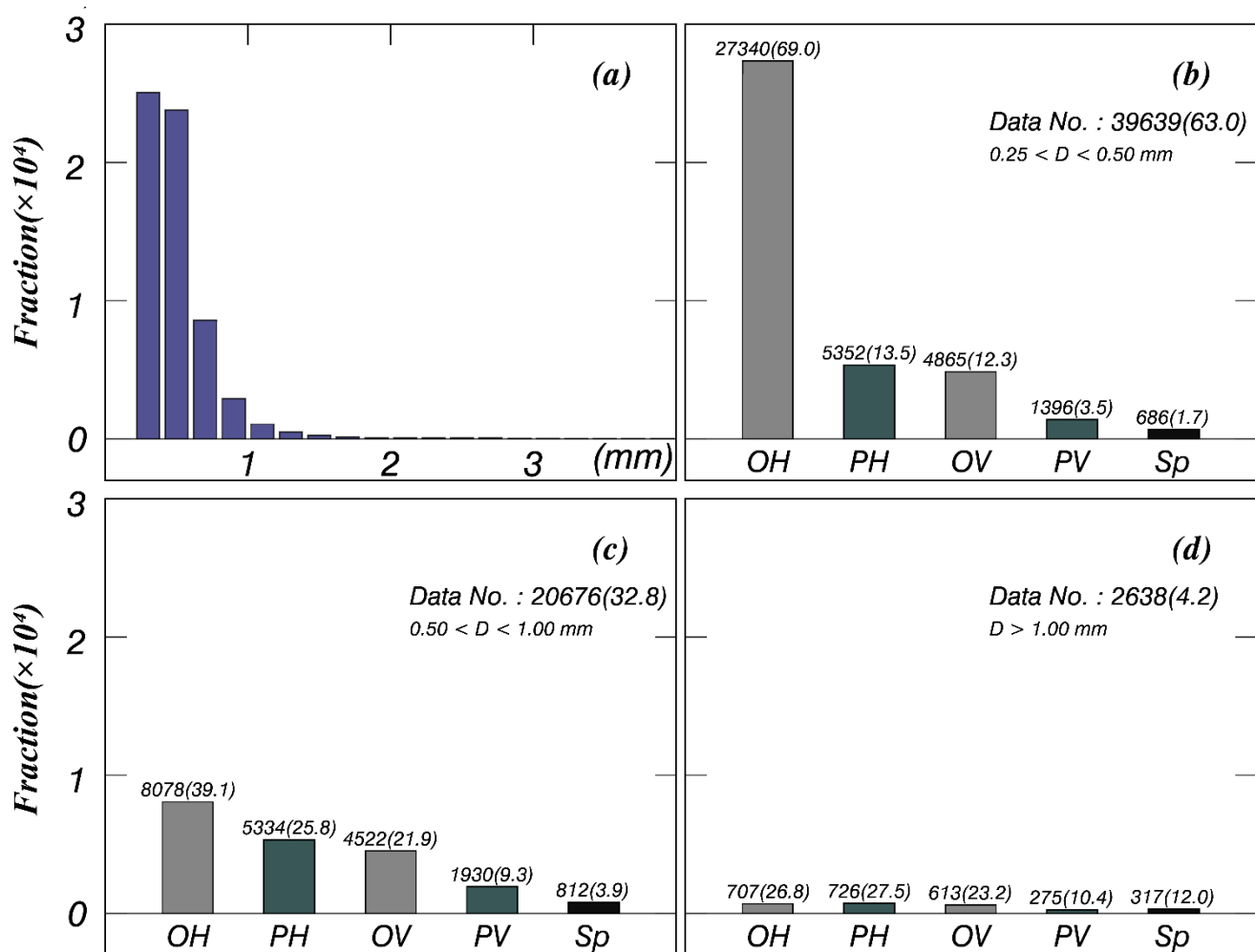
Figure 6. The 1-min interval time series of  $D$  and the number of particles in the free-fall experiment conducted at the NIED.



771

772 Figure 7. Contour image of volcanic ash particles for (a) the axis ratio ( $\gamma$ ) and (b) terminal velocity  
 773 ( $V_T$ ) with respect to the sample. The red solid line is the averaged  $\gamma$  satisfying the condition that the  
 774 correlation coefficient exceeds 0.95. Grey solid line is the relationship of volcanic ash particles  
 775 suggested by Bonadonna et al. (2011).

776



777

778

779

780

781

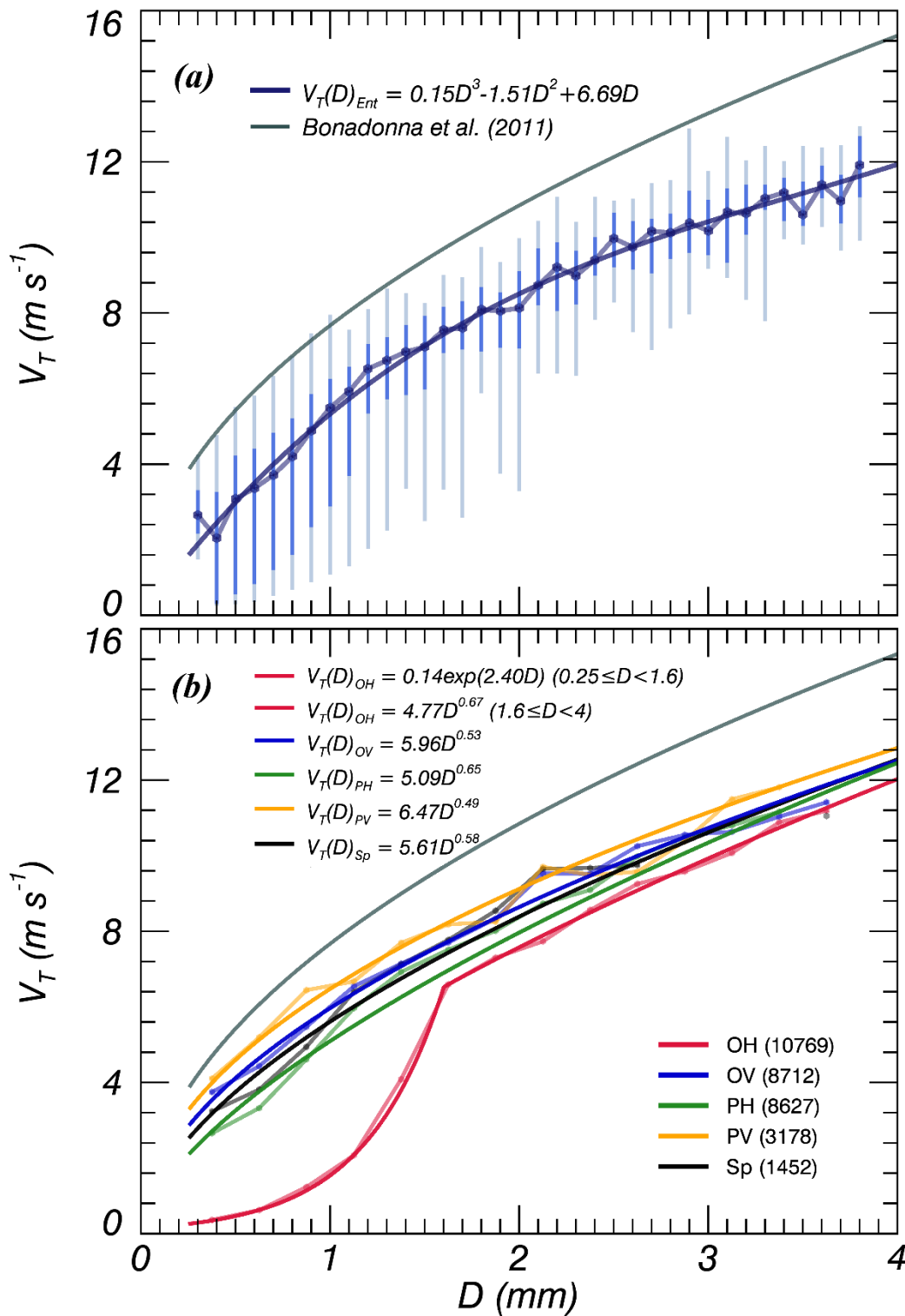
782

783

784

785

Figure 8. Histograms of volcanic ash particles for (a) all particle types and (b–d) each particle shape type of the phi scale. The grey- and dark grey-shaded (patterned) bars indicate horizontal oblate (OH) (vertical oblate [OV]) and horizontal prolate (PH) (vertical prolate [PV]), respectively. The black bar corresponds to spherical (Sp) particles. The number on the top of each bar plot is the number of data points and that in parenthesis is the percentage for each phi scale.



786

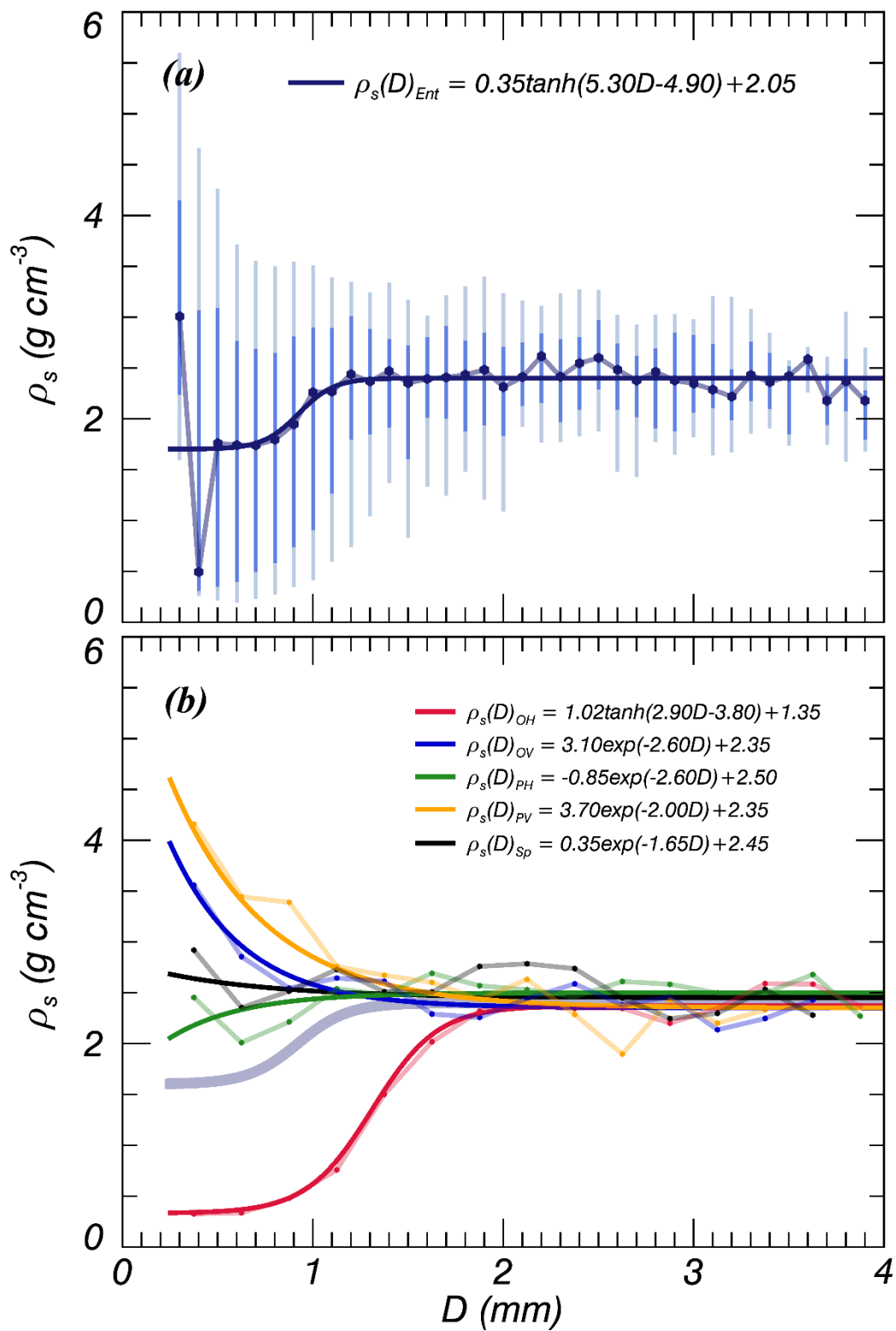
787

788

789

790

Figure 9. Distribution of (a) quartile and (b) median terminal velocity ( $V_T$ ) values after applying the 60%  $V_T$  QC threshold for all and each individual particle shape type, respectively. The grey solid line shows the relationship of volcanic ash particles suggested by Bonadonna et al. (2011).

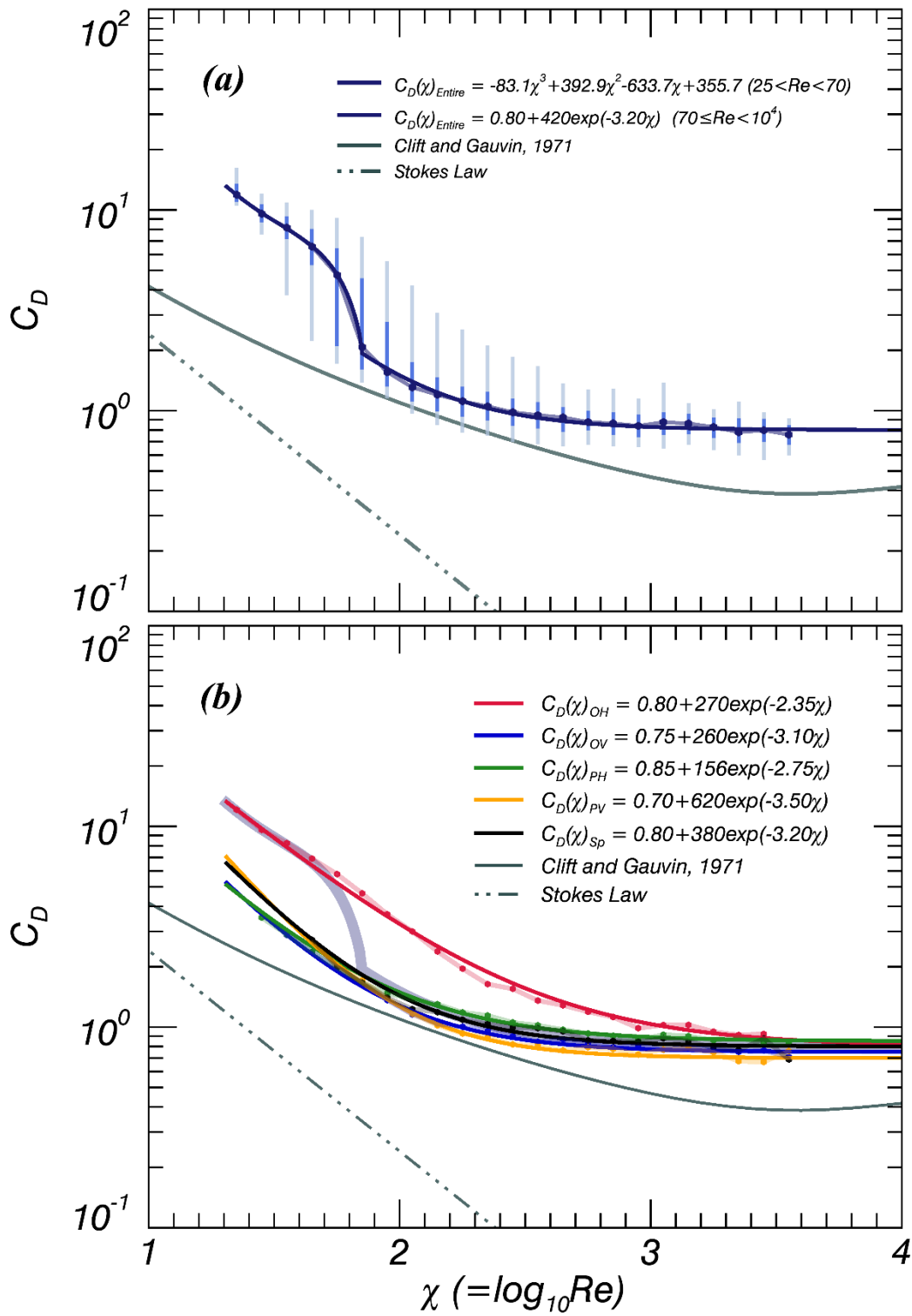


792

793

Figure 10. Same as Fig. 9 but for particle density ( $\rho_s$ ).

794



795

796

797

798

799

Figure 11. Same as Fig. 9 but for Reynolds number ( $Re$ ) and drag coefficient ( $C_D$ ). The grey solid and broken lines in (a) are the relationships of spheres suggested by Clift and Gauvin (1971) and Stokes (1851), respectively.

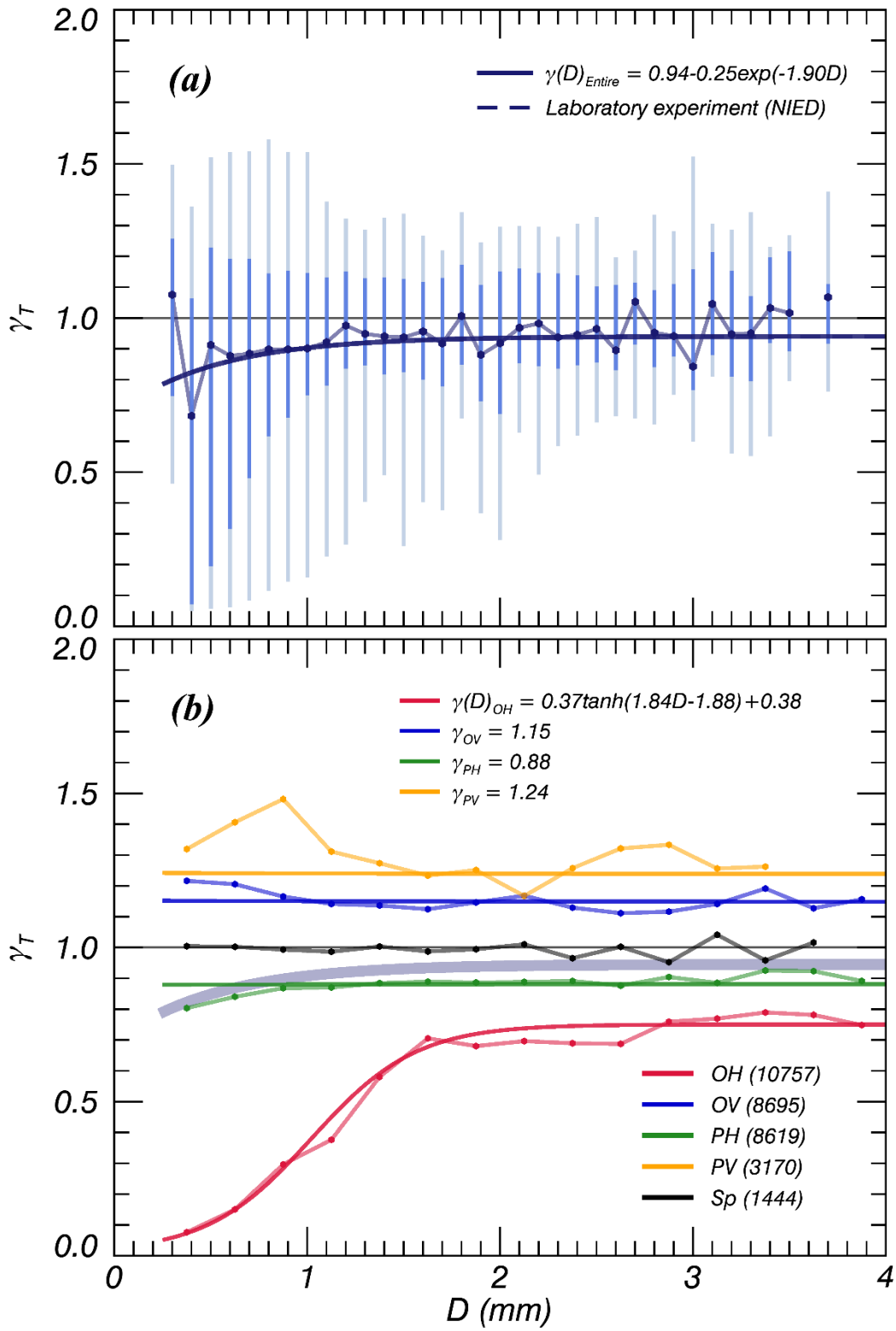
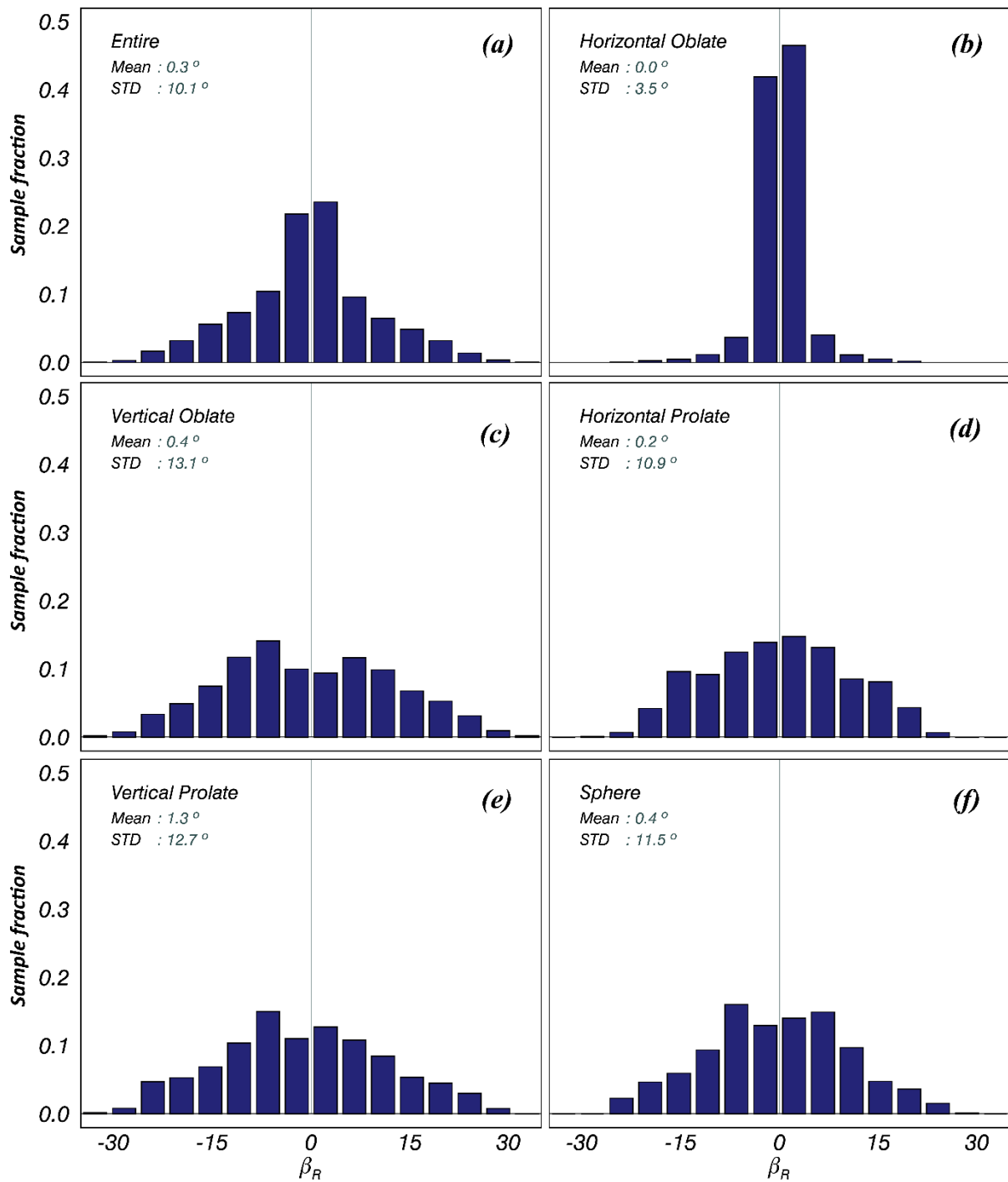


Figure 12. Same as Fig. 9 but for  $\gamma$ .

800  
 801  
 802

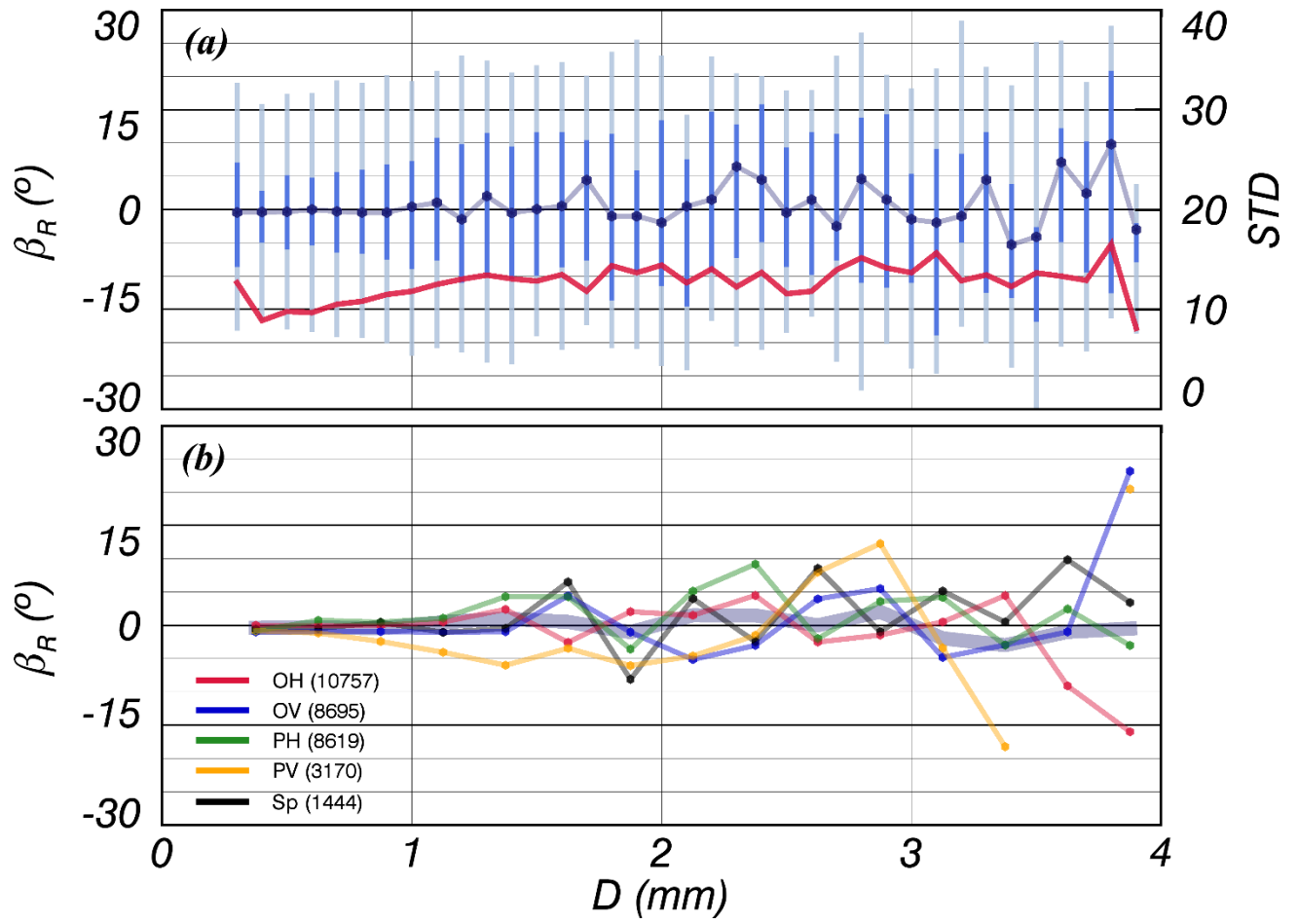




803

804 Figure 13. Histograms of representative canting angle ( $\beta_R$ ) for each particle shape type, including  
 805 the data for all particles.

806



807

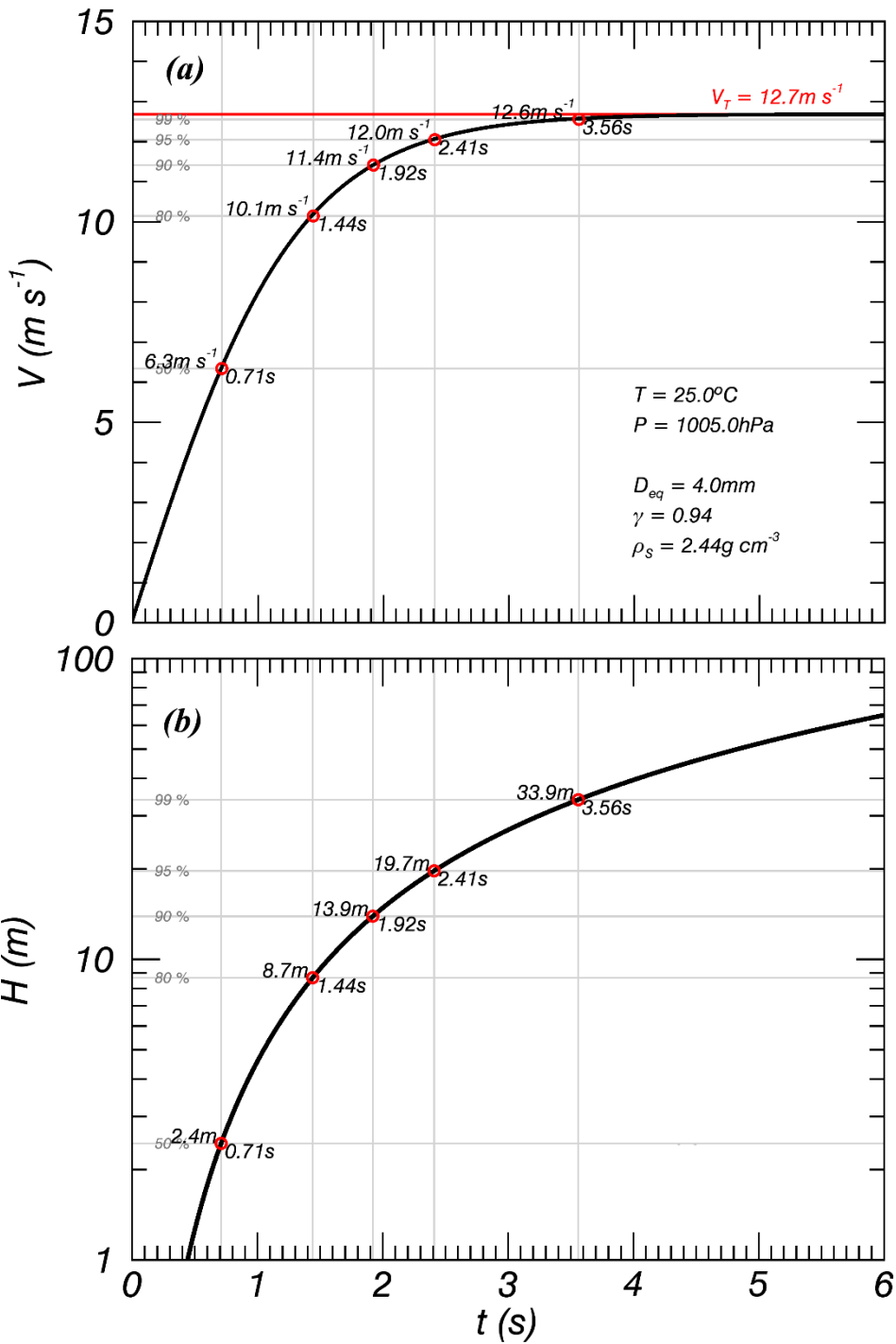
808 Figure 14. Distribution of  $\beta_R$  with  $D$  for each particle shape type including the data for all particles.

809 The red solid line indicates the standard deviation.

810

811

812



813

814 Figure A1. Theoretical (a) fall velocity and (b) falling height for a spheroid with  $D = 4 \text{ mm}$ ,

815 considering the surface roughness coefficient of the volcanic ash particle ( $1.07^{-1}$ ) relative to its fall

816 velocity (Bagheri and Bonadonna, 2016).

817

818 **Tables**

819

820 Table 1. Ash particle classification criteria.

<b>Type</b>	<b>Description</b>	<b>Classification conditions</b>
OH	Horizontal oblate	$\gamma_{T_{1(2)}} < 0.9$ $ \gamma_{T_1} - \gamma_{T_2}  \leq 0.1\gamma_T$
OV	Vertical oblate	$0.9 \leq \gamma_{T_{1(2)}} \leq 1.1,$ $\gamma_{T_{2(1)}} > 1.1$
PH	Horizontal prolate	$ \gamma_{T_1} - \gamma_{T_2}  > 0.1\gamma_T$
PV	Vertical prolate	$\gamma_{T_{1(2)}} > 1.1$ $ \gamma_{T_1} - \gamma_{T_2}  \leq 0.1\gamma_T$
Sp	Sphere	$0.9 \leq \gamma_{T_{1(2)}} \leq 1.1$ $ \gamma_{T_1} - \gamma_{T_2}  \leq 0.1\gamma_T$

821

822 Table 2. Information on the collected volcanic ash particles.

<b>Data</b>	<b>Collection date</b>	<b>Period of free fall experiment (June 18, 2014)</b>	<b>Condition of free fall</b>
<b>A</b>	Dec. 1–31 2008	10:00–12:34 (154 min)	Size by size (phi scale)
<b>B</b>	Mar. 1–31 2010	13:43–14:53 (70 min)	Size by size (phi scale)
<b>C</b>	Feb. 28, 2014	15:11–16:17 (66 min)	Mixed
<b>D</b>	Mar. 31, 2014	16:19–17:05 (46 min)	Mixed
<b>E</b>	Apr. 30 2014	17:07–18:00 (53 min)	Mixed

823

824

825 Table 3. Relationships of terminal velocity with the number of data points, the value of the  
 826 correlation coefficient (CC) and the root mean square error (RMSE) after applying the 60%  $V_T$  QC  
 827 threshold for each particle shape type.

Type	Data number (%)	Relationship ( $0.25 < D \text{ (mm)} \leq 4$ )	CC	RMSE
All	32685 (100)	$V_T(D) = 0.15D^3 - 1.51D^2 + 6.69D$	0.56	1.22
OH	10757 (33)	$V_T(D) = 0.14\exp(2.40D)$ ( $0.25 \leq D < 1.6$ )	0.94	0.46
		$V_T(D) = 4.77D^{0.67}$ ( $1.6 \leq D < 4$ )		
OV	8695 (27)	$V_T(D) = 5.96D^{0.53}$	0.75	0.85
PH	8619 (26)	$V_T(D) = 5.09D^{0.65}$	0.87	0.74
PV	3170 (10)	$V_T(D) = 6.47D^{0.49}$	0.71	0.96
Sp	1444 (4)	$V_T(D) = 5.61D^{0.56}$	0.91	0.78

828